Contributions to Mineralogy and Petrology (2026) 181:94
https://doi.org/10.1007/s00410-026-02346-5

ORIGINAL PAPER

From partial melting to pluton emplacement: insights from zircon and titanite petrochronology of the El Oro complex, Ecuador

Hugo Dominguez[1,2,3] · Renée Tamblyn[1,4] · Mahyra Tedeschi[5,6] · Nicolas Riel[3] · Jacob B. Forshaw[7] · Etienne Jaillard[8] · Samuel Macías-Mosquera[9] · Pierre Lanari[1,4]

Received: 3 November 2025 / Accepted: 3 July 2026
© The Author(s) 2026

Abstract

Partial melting of the lower continental crust during high-temperature, low-pressure metamorphism is commonly associated with the emplacement of felsic plutons in the middle to upper crust. However, the duration and conditions of anatexis, melt extraction, and emplacement processes in these settings remain uncertain. The El Oro Complex in southern Ecuador preserves a kilometre-scale, tilted crustal section comprising a structurally continuous Triassic sequence of metamorphosed sedimentary rocks and associated S-type granitoids. A large number per sample of combined in situ zircon U–Pb dates and trace-element compositions has been obtained by laser ablation inductively coupled plasma mass spectrometry (LA-ICP-MS) from both migmatites in the lower paleo-crust and granitoids in the middle to upper paleo-crust. This approach, combined with cathodoluminescence imaging, is used to distinguish different zircon populations within individual samples beyond U–Pb analytical uncertainty. All samples from both migmatites and granitoids mostly record zircon crystallisation ages between ca. 240 and 225 Ma. In the migmatites, trace-element heterogeneity in zircon is observed at the sample scale. Depending on the sample, this variability reflects either changes in the melting reactions or open-system behaviour involving melt influx from other sources at the scale of individual leucosomes. U–Pb dates and Zr-thermometry data from titanites using LA-ICP-MS were also collected from the Piedras metagabbro, commonly interpreted as the heat source for the sequence's metamorphism. Titanite grains record a consistent age of 227.5 ± 4.5 (n = 94) Ma with a temperature of ~720–740 °C, and are interpreted as dating the cooling of the gabbro emplacement related to the end of metamorphism. Together, these data confirm the co-genetic link between the migmatites and the granitoids of the El Oro complex and the interpretation that the Piedras unit is the main heat source for the metamorphism. This study showcases important trace-element variability in zircons at the sample scale, both in migmatites and granitoids, reflecting the interplay between partial melting, melt extraction, and subsequent crystallisation.

Keywords Zircon · Anatexis · Petrochronology · Granitoids · Migmatites · El Oro complex

Communicated by Hans Keppler.

✉ Hugo Dominguez
hdomingu@uni-mainz.de

1 Institute of Geological Sciences, University of Bern, Baltzerstrasse 3, Bern 3012, Switzerland

2 Institute of Multiscale Modelling (M3ODEL), 55099 Mainz, Germany

3 Institute of Geosciences, Johannes Gutenberg University, 55099 Mainz, Germany

4 Institute of Earth Sciences, University of Lausanne, Géopolis, Lausanne 1015, Switzerland

5 Geological Survey of Finland, Espoo 02151, Finland

6 Programa de Pós-Graduação em Geologia, Universidade Federal de Minas Gerais, CPMTC-IGC, Campus Pampulha, Belo Horizonte, Brazil

7 Mineral Deposit Research Unit, Department of Earth, Ocean and Atmospheric Sciences, University of British Columbia, 2207 Main Mall, V6T 1Z4 Vancouver, Canada

8 Université Grenoble Alpes, ISterre, IRD UR 219, CNRS UMR 5275, CS 40700, Cedex 9, Grenoble 38058, France

9 Facultad de Ciencias Naturales, Universidad de Guayaquil, Guayaquil 090601, Ecuador

Published online: 02 November 2026

Introduction

The processes of melt production, segregation, and emplacement are fundamental to understanding the evolution of the continental crust. These processes govern the formation of migmatites and granitoids, which record the history of crustal growth, reworking, and heat transfer (Vielzeuf et al. 1990; Hawkesworth et al. 2010; Jaupart and Mareschal 2010; Korenaga 2018). A key challenge is to constrain the timescales and conditions under which melting and emplacement occur in crustal-dominated settings (Brown 2013). This is difficult because the high temperatures involved reset most available radiometric systems through diffusion, obscuring not only the final stage of cooling but also earlier events such as successive melt injections or episodes of crustal reworking. Zircon is a well-established exception: it preferentially crystallises from melt, has very high closure temperatures for Pb and other trace element (>900 °C), is resistant to late disturbance, and is able to record different snapshots during the processes involving melt production and emplacement (Cherniak et al. 1997; Cherniak and Watson 2001; Rubatto 2017; Bloch et al. 2022). As such, zircon petrochronology has appeared as a powerful approach that can provide precise temporal and geochemical constraints to elucidate the complex interplay between magmatic and metamorphic melting processes (e.g. Oliver et al. 1993; Michel et al. 2008; Wu et al. 2011; Schoene et al. 2012; Samperton et al. 2015; Farina et al. 2018).

For plutonic systems, high-precision isotope-dilution, thermal ionization mass (ID-TIMS) zircon geochronology has shown that magma reservoirs are incrementally constructed zones over timescales of 10^5-10^6 years (Kemp et al. 2007; Michel et al. 2008; Schoene et al. 2012; Wotzlaw et al. 2013; Samperton et al. 2015; Cashman et al. 2017). These timescales correlate positively with pluton size, implying broadly similar magmatic fluxes across tectonic settings (De Saint Blanquat et al. 2011). Consequently, magma transfer and pluton emplacement appear to occur on shorter timescales than tectonic rates (Petford et al. 2000; Annen 2011; De Saint Blanquat et al. 2011; Van Zalinge et al. 2022). However, most such studies focus on arc or intraplate environments, where magmas reflect mantle-crust mixing (e.g. Szymanowski et al. 2015; and previous references). In contrast, the timing and timescale of purely crustal-derived, peraluminous granitoids remain poorly constrained (Farina et al. 2014, 2018).

In the deeper crust, melt production is subject to different controls. Partial melting driven by metamorphic dehydration reactions depends chiefly on temperature, and thus the duration of prograde metamorphism (Winter 2014). Typical timescales of melt production are closer to tectonic rates, on the order of tens of millions of years for regional metamorphism, but can be shorter, depending on the heat source and setting (e.g. Rubatto et al. 2001, 2013; Harris et al. 2004; Gordon et al. 2008, 2010; Weinberg 2016; Oldman et al. 2025). The apparent mismatch between slow deep-crustal melting and rapid pluton emplacement raises fundamental questions about melt extraction and transfer through the crust.

Direct comparisons of granitoid plutons and their potential migmatitic sources are rare (e.g. Reichardt and Weinberg 2012; Li et al. 2022) because melting generally occurs deep in the continental crust, whereas plutons are emplaced in the middle to upper crust (Sawyer et al. 2011). The El Oro complex in southern Ecuador provides an exceptional opportunity to bridge this gap. This tilted crustal section of metasediments from the Ecuadorian fore-arc exposes both migmatites and associated S-type granitoids over ~20 km, representing a complete crustal profile from source to emplacement level (e.g. Feininger 1978, 1982; Baldock 1982; Litherland 1994; Gabriele 2002; Riel et al. 2013).

Here, we present zircon U–Pb geochronology and trace-element data from migmatites and S-type granitoids of the El Oro complex, along with titanite ages from the associated metagabbro, interpreted as the heat source. Although TIMS and secondary-ion mass spectrometry (SIMS) provide high-precision U–Pb zircon ages, these methods are limited in the ability to obtain trace-element data from the same location within a grain and/or to collect a high number of analyses per session. Here, we evaluate the potential of using quadrupole LA-ICP-MS for acquiring a large number of U–Pb and trace-element analyses, each obtained simultaneously from a single ablation volume. This is comparatively cost-effective with shorter data acquisition times than SIMS or TIMS, at the cost of lower analytical precision, and do not require laser-ablation split-stream (i.e. Kylander-Clark et al. 2013). The interpretation of the results confirm that granitoid emplacement was synchronous with prograde metamorphism and occurred through multiple intrusive pulses over several million years. By combining large zircon datasets with trace-element systematics, we distinguish zircon populations that record melt generation, open-system processes, and crystallisation histories, thereby constraining the temporal coupling between crustal melting and pluton assembly.

Geological settings and previous studies

The El Oro complex (EOC) is located in southern Ecuador and encompasses ~1500 km^2. It is bordered to the south by the Cretaceous Celica-Lancones sedimentary basin, to the east by Tertiary volcano-detrital deposits, and to the north by the Raspas complex, a metamorphosed ophiolite complex. It can be separated into three major groups, from south to

north: the metamorphic continental sequence of the Tahuín group, the amphibolitised metagabbro of the Piedras unit, and the blueschists of the Arenillas-Panupalí unit (Fig. 1). The Tahuín group comprises mostly clastic sediments interpreted to have been deposited on a passive margin; these are now exposed as a section of tilted continental crust preserving an increasing degree of metamorphism from south to north (Feininger 1982; Aspden et al. 1995; Vinasco Vallejo 2004; Riel et al. 2013). The age of deposition of the sediments at the top of the sequence is poorly constrained, with available evidence suggesting an Ordovician to Carboniferous age. This is based on scarce palaeontological evidence mostly found on the equivalent sequence on the Peruvian side of the Amotape massif (Iddings and Olsson 1928; Martínez 1970; Mourier 1988; Aspden et al. 1995; Cózar et al. 2024), and from the depositional age of detrital zircons in the (meta)sediments of the sequence (Suhr et al. 2019). The Tahuín group is separated from the rest of the EOC by a large-scale normal fault, but a magmatic contact has been observed in some localities with the metagabbroic Piedras unit (Riel et al. 2013). Different nomenclatures have been used over time to describe the Tahuín group (e.g. Feininger 1978; Baldock 1982; Aspden et al. 1995). We follow the nomenclature defined in Riel et al. (2013), which is based on Aspden et al. (1995), but redefine the La Bocana unit as metamorphic rather than plutonic.

Three sub-units are defined, following major metamorphic isograds. The El Tigre unit consists of unmetamorphosed to greenschist facies sediments, predominantly composed of turbidites (Aspden et al. 1995). The La Victoria unit, here separated from El Tigre by the Biotite-in isograd, is composed of a sequence of metapelites and metapsammites preserving increasing degrees of metamorphism up to amphibolite facies (Feininger 1978). The La Bocana unit is characterised by the beginning of partial melting and is composed of migmatites. Riel et al. (2013) divide this unit into two parts: Upper La Bocana, characterised by the presence of metatexites, and Lower La Bocana, defined by the Garnet-in isograd, composed mainly of diatexites. Riel et al. (2013)report two zircon $^{206}Pb/^{238}U$ ages: 225.7±6.5 (MSWD=2.6, n=12) and 229.3±2.4 Ma (MSWD=0.96, n=5), and two monazite $^{208}Pb/^{232}Th$ ages at 226.0±1.3 (MSWD=2.44, n=17) and 223.22±2.2 Ma (MSWD=1.71, n=11) in the Lower La Bocana unit that

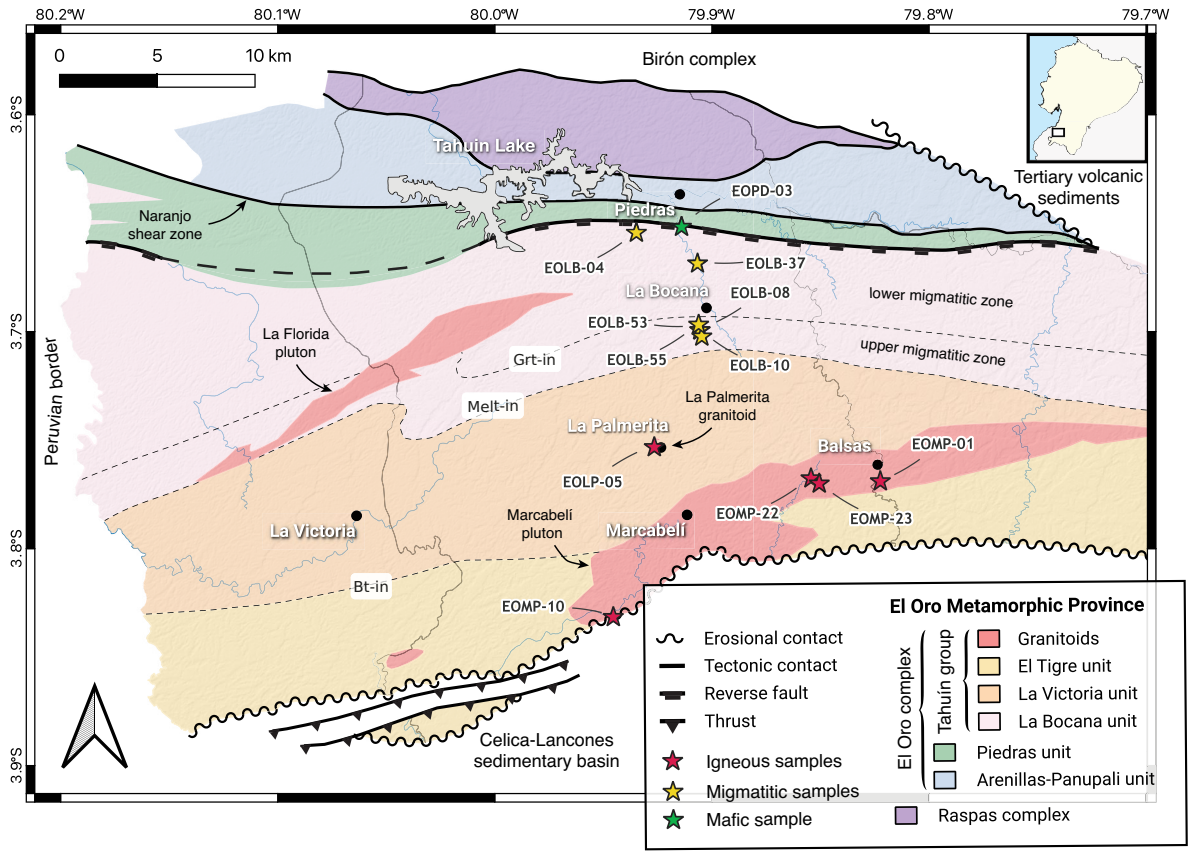


Fig. 1 Simplified geological map of the western part of the El Oro metamorphic province. The stars represent the position of the samples used in this study.

constrain the melting event (Table 1). $^{40}Ar/^{39}Ar$ dating on muscovite yields 218.18 ± 0.94 (MSWD = 1.47, n = 7) and 214.56 ± 0.93 (n = 10) (Cochrane 2013; Spikings et al. 2015; Paul et al. 2018) and records the cooling of the Lower La Bocana unit (Table 1).

The geodynamic heat source for the metamorphism of the Tahuín group is attributed to the emplacement of the Piedras unit gabbro (Riel et al. 2013). The gabbro is amphibolitised and $^{40}Ar/^{39}Ar$ dating on hornblende yields ages, within uncertainty, of the $^{206}Pb/^{238}U$ ages from magmatic zircon

Table 1 Compilation of the available geochronological data in the El Oro complex linked to the Triassic metamorphic event

Geological unit	Lithology	Age [Ma]	Mineral analysed	Analytical method	Interpretation (this study)	Reference
Marcabelí pluton	Granitoid	227.5 ± 0.8 (MSWD = 0.013 (R), n = 3)	Monazite	$^{207}Pb/^{235}U$ using TIMS	Magmatic crystallisation	Noble et al. (1997)
	Granitoid	234.9 ± 4.5 (MSWD = 0.64, n = 6)	Zircon	$^{206}Pb/^{238}U$ using SHRIMP	Magmatic crystallisation	Vinasco Vallejo (2004)
La Florida pluton	Granitoid	239.6 ± 7.3 (MSWD = 1.3, n = 9) 215.5 ± 7.8 (MSWD = 0.35, n = 3)	Zircon	$^{206}Pb/^{238}U$ using SHRIMP	Magmatic crystallisation	Vinasco Vallejo (2004)
Lower La Bocana	Migmatite	225.7 ± 6.5 (MSWD = 2.6 (R), n = 12) 229.3 ± 2.4 (MSWD = 0.96 (R), n = 5)	Zircon	$^{206}Pb/^{238}U$ using SHRIMP	Anatectic melt crystallisation	Riel et al. (2013)
	Migmatite	226.0 ± 1.3 (MSWD = 2.44 (R), n = 17) 223.2 ± 2.2 (MSWD = 1.71 (R), n = 11)	Monazite	$^{208}Pb/^{232}Th$ using LA-ICP-MS	Anatectic melt crystallisation	Riel et al. (2013)
	Migmatite	232.2 ± 5.1 (MSWD = 0.029, n = 6)	Zircon	$^{206}Pb/^{238}U$ using SHRIMP	Anatectic melt crystallisation	Vinasco Vallejo (2004)
	Metagranite	227.1 ± 1.9	Zircon	$^{206}Pb/^{238}U$ using LA-ICP-MS	Anatectic melt crystallisation	Paul et al. (2018)
	Metagranite	237.7 ± 5.2 (MSWD = 4.6, n = unknown)	Zircon	$^{206}Pb/^{238}U$ using LA-ICP-MS	Anatectic melt crystallisation	Cochrane (2014)
	Metagranite	218.18 ± 0.94 (MSWD = 1.47, n = 7)	Muscovite	$^{40}Ar/^{39}Ar$ using stepped heating procedure	Cooling	Paul et al. (2018)
	Metagranite	214.56 ± 0.93 (n = 10)	Muscovite	$^{40}Ar/^{39}Ar$ using stepped heating procedure	Cooling	Cochrane (2014)
Piedras	Metagabbro	221 ± 18 (MSWD = 0.015 (R), n = 2)	Zircon	$^{206}Pb/^{238}U$ using TIMS	Magmatic crystallisation	Noble et al. (1997)
	Metagabbro	222.7 ± 6.3 (MSWD = 1.90, n = 17)	Zircon	$^{206}Pb/^{238}U$ using LA-ICP-MS	Magmatic crystallisation	Cochrane et al. (2014)
	Metagabbro	226 ± 1.8	Hornblende	$^{40}Ar/^{39}Ar$ using stepped heating procedure	Retrograde metamorphism	Gabriele (2002)
Arenillas-Panupalí	Blueschists	225.3 ± 1.7	Hornblende	$^{40}Ar/^{39}Ar$ using stepped heating procedure	Retrograde metamorphism	Gabriele (2002)

When not available in the original publication, and when possible, the MSWD was recalculated and is indicated by the letter R

of the same unit, around 226 to 222 Ma (Noble et al. 1997; Gabriel, 2002; Cochrane et al. 2014; Table 1). This indicates that the emplacement and amphibolitisation of the gabbro occured in a relatively short succession, suggesting rapid cooling. This rapid cooling is attributed to the underthrusting of the comparatively cool blueschists of the Arenillas-Panupalí unit, which records similar $^{40}Ar/^{39}Ar$ ages and peak metamorphic *P–T* conditions of ~0.9 GPa and 300 °C (Gabriele 2002; Table 1). Metamorphism and partial melting of the Tahuín group rapidly ceased as a result.

In the western part of the EOC, the units of the Tahuín group are intruded by granitoids, with two major plutons: the La Florida pluton, intruding the La Bocana unit, and the Marcabelí pluton, intruding the La Victoria and El Tigre units (Aspden et al. 1995; Noble et al. 1997; Vinasco Vallejo 2004; Fig. 1). Vinasco Vallejo (2004) obtained a zircon $^{206}Pb/^{238}U$ age of 234.9±4.5 (MSWD=0.64, n=6) Ma for the Marcabelí pluton, and two ages of 239.6±7.3 Ma (MSWD=1.3, n=9) and 215.5±7.8 Ma (MSWD=0.35, n=3) for the La Florida pluton, supporting a coeval relationship with the Triassic metamorphic event recorded in the Tahuín group (Table 1). The Marcabelí pluton is one of the focuses of this study and is a heterogeneous body which presents a variety of facies, from medium to coarse-grained monzogranites and granodiorites (Fig. 2a). Like the La Florida pluton, it has an S-type affinity, but the presence of hornblende and mafic microgranular enclaves in some localities also suggests contamination by a mafic source (Fig. 2a-b; Aspden et al. 1995; Vinasco Vallejo 2004).

Sampling strategy and sample description

Selecting representative samples for studying melt processes is inherently challenging because melting and crystallization generate strong chemical heterogeneities at all scales in both migmatites and plutons. To address this, we focused on leucosomes from neosomes or diatexites within migmatites, as these are most likely to represent late-melt crystallisation, and consequently, pathways of melt extraction. For the granitoids, we targeted a variety of lithologies to capture potential temporal or compositional variations among distinct magmatic phases. Sampling was carried out along a general south–north transect across the Tahuín Group, interpreted as a tilted crustal section from shallow to deep levels. This approach aimed to test possible co-genetic relationships between the migmatites and associated granitoids.

In total, five granitoid samples were collected: four samples from the Marcabelí pluton (EOMP-01, EOMP-10, EOMP-22, EOMP-23) and one from a small isolated granitoid body near La Palmerita (EOLP-05), hereafter referred to as the La Palmerita granitoid. Six migmatite samples were also collected: two leucosomes (EOLB-08, EOLB-10) and two diatexites (EOLB-53, EOLB-55) from the Upper La Bocana unit, and two diatexites were obtained from the Lower La Bocana unit (EOLB-04, EOLB-37). The Upper La Bocana unit was specifically targeted because it is interpreted as the final melting front of the heat anomaly event (Riel et al. 2013), and lacks previous geochronological constraints.

Brief petrographic descriptions of all samples are provided below, and their locations are shown in Fig. 1. GPS coordinates are provided with the analytical data (see data availability). Mineral abbreviations follow Warr (2021), and migmatite terminology follows Sawyer (2008).

Igneous samples

Marcabelí pluton

As the Marcabelí pluton is a heterogenous body, four samples, divided into three groups, have been investigated. These groups are: medium-grained quartz-rich monzogranite, referred to as muscovite-bearing quartz monzonite (samples EOMP-01 and EOMP-23), coarse-grained monzogranite, referred to as monzogranite (sample EOMP-10), and coarse-grained granodiorite, referred to as hornblende-bearing granodiorite (sample EOMP-22) based on their occurrences of K-feldspar and quartz (Fig. 2c). The samples all contain quartz, plagioclase, K-feldspar, and biotite. Chlorite often replaces biotite. The muscovite quartz monzonite (sample EOMP-23) is the only igneous sample where a titanium-bearing phase was observed (titanite).

La Palmerita granitoid

The La Palmerita granitoid constitutes a homogeneous granitoid body containing accessory muscovite and sillimanite, with a few biotite-rich enclaves. One representative sample (sample EOLP-05) was selected for analysis. It is a medium-grained muscovite- and sillimanite-bearing monzogranite. The Ti-bearing accessory phases are ilmenite and titanite.

Migmatite samples

Upper La Bocana unit

The outcrops of the four samples (EOLB-08, EOLB-10, EOLB-53, EOLB-55) collected in Upper La Bocana show a variety of migmatitic textures on a scale of hundreds of metres, ranging from stromatic metatexites (Fig. 2d) with centimetre-scale layers to diatexites with dominant

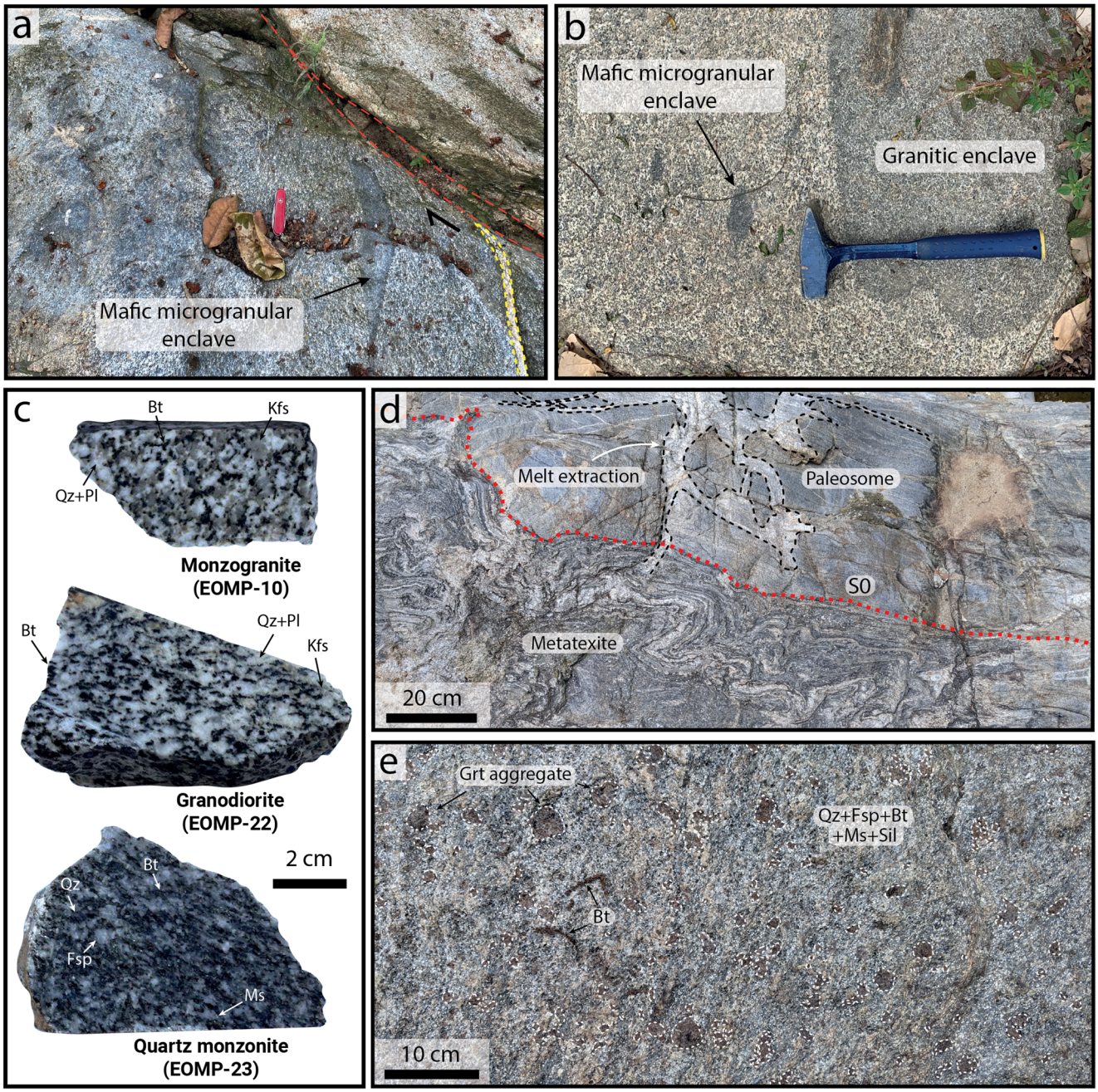


Fig. 2 Representative field and sample photos from the Marcabelí pluton and migmatites of the La Bocana unit. **a** Locality showing two types of granitoids in the Marcabelí pluton. The melanocratic granitoid shows kinematic indicators of deformation in contact with the leucocratic granitoid, as highlighted by the yellow dotted contour around a quartz vein. The leucocratic granitoid is interpreted as posterior to the emplacement of the melanocratic granitoid. Note the presence of a mafic microgranular enclave. **b** Evidence of magma mingling in the Marcabelí pluton. Locality close to (**a**). **c** Photographs of the granitic samples from the Marcabelí pluton showing the different textures. **d** Outcrop picture of a typical metatexite in Upper La Bocana unit. The paleosome is mainly formed by quartzitic layers, whereas the metatexite is composed of millimetre- to centimetre-scale leucosomes and melanosomes. **e** Outcrop picture of a representative diatexite in Lower La Bocana unit. Garnet aggregates represent an important volume of the rock

leucocratic neosomes. Samples EOLB-08 and EOLB-10 represent leucosome layers from the biotite stromatic metatexites. Samples EOLB-53 and EOLB-55 represent the homogeneous schollen diatexites. The major mineral assemblage of the four samples is quartz, plagioclase, K-feldspar, biotite, and muscovite. Apatite, zircon, monazite, ilmenite, titanite, and rutile occur as accessory phases. Representative micrographs for the diatexite and leucosomes from the metatexite samples are provided in the supplementary material (Fig. S1a and S1b).

Lower La Bocana unit

Samples EOLB-04 and EOLB-37 represent diatexites composed mainly of quartz, plagioclase, K-feldspar, biotite, muscovite, garnet, and sillimanite (Fig. 2e). Millimetre- to centimetre-scale garnet poikiloblasts are present in both samples and are often rimmed by biotite. Both samples contain graphite, apatite, zircon, monazite, ilmenite and rutile as accessory phases; titanite is additionally present in EOLB-04. A representative micrograph is provided in the supplementary material (Fig. S1c).

Metagabbro sample

Piedras metagabbro

Sample EOPD-03 is a medium-grained amphibolite containing mainly hornblende (~70–75%) and altered plagioclase (~20–25%) with titanite as a minor phase (~2–5%). Quartz is present as an accessory phase, and rutile and zircon were found as inclusions in titanite. A representative micrograph is provided in supplementary material (Fig. S1d).

Analytical methods

Sample preparation and imaging

Samples were cut into small blocks, disaggregated using a high-voltage SelFrag device at the University of Bern, and then sieved. Zircon and titanite grains were extracted from the 65–250 and 250–500 µm fractions, respectively, using standard density and magnetic separation techniques, including a Frantz isodynamic magnetic separator and heavy liquid methylene iodide. Hand-picked zircons and titanites were mounted in epoxy and polished to expose their mid-sections. Imaging was conducted on two different instruments: a ZEISS EVO50 scanning electron microscope (SEM) and a ZEISS SIGMA 560VP at the Institute of Geological Sciences, University of Bern. For zircon, charge contrast (CC) imaging was performed on a ZEISS EVO50 under low vacuum conditions (18 Pa) with an accelerating voltage of 12 kV, a beam current of 700–750 pA, and a working distance of 10–11 mm. Cathodoluminescence (CL) imaging was performed with the ZEISS SIGMA 560VP using an accelerating voltage of 15 kV and a similar working distance. Charge contrast and CL images produced equivalent results. For titanite grains, back-scattered electrons (BSE) images were acquired on the ZEISS SIGMA 560VP using an accelerating voltage of 15 kV and a working distance of 10–11 mm.

Zircon and titanite U–Pb and trace element analyses

Zircon U–Pb and trace elements were collected simultaneously using a RESOlution-LR 193 nm excimer laser ablation system (Applied Spectra), with a S155 sample chamber (Laurin Technic), coupled to an Agilent 7900 ICP-MS housed at the University of Bern. Measurements were conducted across six sessions. Zircons were ablated at a surface energy density (or fluence) of 2.5 J cm^{-2} at a repetition rate of 5 Hz, with laser spot diameters of 16 and 30 µm, with three pulses of pre-cleaning ablation. Analyses included 30 s of background, followed by 30 s of ablation, and 20 s of washout time. Titanite grains were ablated at a surface energy density (or fluence) of 3 J cm^{-2} at a repetition rate of 5 Hz, and a laser spot diameter of 50 µm, with three pulses of pre-cleaning ablation. Analyses comprised 30 s of background, followed by 40 s of ablation, and 20 s of washout time. He was the carrier gas (at 400 mL min^{-1}), and N_2 (at 3.5 mL min^{-1}) was added to the carrier gas after the sample chamber to increase sensitivity. The measured masses and their corresponding dwell times are detailed in Table S1 for each session. All LA-ICP-MS data were processed using the software LADR (Norris and Danyushevsky 2018) to correct for gas backgrounds, downhole fractionation and instrument mass bias and drift. Background measurements were subtracted from the analysis using a step function, while U–Pb isotopic ratios and trace elements were corrected for using polynomial fits. Downhole fractionation corrections were grouped by spot size. For the unknowns, individual uncertainties for trace elements were generally as follows: Ti: 25–40%, Ce: 8–20%, Nd, Sm and Eu: 20–40%, Gd to Lu: 3–17%. The Ti-in-zircon thermometry uncertainties include the measurement uncertainty, and those are presented on figures where this data is shown.

The primary reference material (PRM) for zircon U–Pb calibration was GJ-1, which has a $^{206}Pb/^{238}U$ age of 600.7 ± 1.1 Ma (Jackson et al. 2004). Secondary reference materials included Plešovice, which has a $^{206}Pb/^{238}U$ age of 337.13 ± 0.37 Ma (Sláma et al. 2008) and 91500, which has a $^{206}Pb/^{238}U$ age of 1062.4 ± 0.4 Ma (Wiedenbeck et al. 1995). The Plešovice standard was used as a secondary reference standard for 16 µm spots only, as 30 µm spots produced high U counts, which often shifted the ICP-MS detector from pulse to analog mode, and had correspondingly high U/Pb ratios. This may have induced different downhole fractionation effects which could not be accounted for by using the lower U content GJ-1 PRM. Plešovice was also monitored for across-session reproducibility, as discussed below. Over the course of the six sessions, Plešovice returned a weighted mean $^{206}Pb/^{238}U$ age of 339.46 ± 0.64/3.83 Ma (MSWD = 1.43, n = 169) and 91500 returned a weighted mean $^{206}Pb/^{238}U$ age

1059.75 ± 1.51/11.27 Ma (MSWD = 0.91, n = 246) (Fig. S2), where the reported uncertainties include without and with systematic uncertainty (see below). The PRM for trace elements was SRM NIST612 or SRM NIST610 (Jochum et al. 2011), and GSD-1G (Jochum et al. 2005) was used for a secondary standard correction in order to correct for spot size effects. Zr was used as the internal element standard for all zircon analyses with a value of 43.14 wt%.

Titanite analyses were limited to one analytical session. The PRM used was MKDE1, which has a $^{206}Pb/^{238}U$ age of 600.7 ± 1.1 Ma (Spandler et al. 2016). The secondary reference materials included BLR (Aleinikoff et al. 2007), which returned a lower intercept discordia age of 1076 ± 34 Ma (MSWD = 5.7). The high uncertainty is attributed to the high U content of the reference material, which leads to low spread along the discordia line. By anchoring the discordia line to the common lead composition determined by the Stacey-Kramers model ($(^{207}Pb/^{206}Pb)_c$ = 0.912) (Stacey and Kramers 1975), a lower intercept age of 1040.1 ± 10.3 Ma was obtained, which is within the uncertainty of the reported TIMS age of 1047.1 ± 0.4 Ma (Aleinikoff et al. 2007). The PRM for trace elements was SRM NIST610, and GSD-1G (Jochum et al. 2005) was used as secondary standard to correct for spot size effects.

Filtering, uncertainties and weighted means of zircon U–Pb

Since the focus of this contribution is the Triassic metamorphic event, all analyses older than 270 Ma were discarded. Care was taken to select earlier time points in the time-resolved laser signals that reflected the targeted domains and to avoid incorporating inherited zircon. Additionally, only concordant data at a 2σ confidence level were considered for the secondary standards and the samples. Concordance was assessed graphically using IsoplotR. As such, all data reported for the samples in this manuscript are concordant within 2σ and < 270 Ma. However, the complete dataset before filtering is included in the supplementary material for the interested reader. The open-source programming language Julia (Bezanson et al. 2017) was used with the Isoplot.jl package (Keller 2023) to compute dates, weighted means, and propagate uncertainties. Systematic uncertainties are propagated into the weighted mean date uncertainties presented in this study, and are obtained by combining in quadrature the random uncertainty, the excess variance (ϵ), the uncertainty of the decay constant and the ratio uncertainty on GJ-1 for the isotopic ratio $^{206}Pb/^{238}U$. To enable comparison of dates across multiple sessions, an estimate of ϵ is needed. This was achieved iteratively by computing a weighted mean from all the 16 µm analyses across the six analytical sessions of this study from Plešovice until the value of MSWD converges to 1 by varying ϵ (see, for instance, Sliwinski et al. 2022). The excess variance was estimated at 1.12% at 2σ across the six sessions.

For each sample, weighted means were calculated using the median absolute deviation (MAD). The median value of the population in each sample is computed, and the absolute deviation of each sample from this median is calculated. The median absolute deviation is then computed as the median of these absolute deviations. Any analysis with an absolute deviation exceeding twice the MAD at 1σ is deemed an outlier and excluded from weighted mean calculations. This was done to obtain a consistent method to compute ages across samples and to remove bias from sample and signal selection as the MAD method is a robust statistical method, meaning that it is insensitive to outliers and departures from normal distribution (Rousseeuw and Croux 1993; Huber and Ronchetti 2009). The dates and ages are reported with two uncertainties at 2σ: without systematic uncertainty propagation and with systematic uncertainty following the guidelines and recommendations for uncertainty propagation and statistics from Horstwood et al. (2016).

Results

Marcabelí pluton and La Palmerita granitoid

Zircon morphology

Zircon grains are colourless, subrounded to euhedral, mostly equidimensional, with a small number being elongated. Their widths range from ~40–100 µm, with lengths varying from ~80–300 µm for aspect ratios ranging from 2 to 5, with up to four or five distinct zones, composed mostly of large cores (Fig. 3). For the samples from the Marcabelí pluton, charge contrast and CL images often show complex zoning with multiple generations of cores and overgrowths (Fig. 3a). CL domains with ages younger than 270 Ma are characterised either by oscillatory zoning with CL-grey response, or by homogeneous rims that appear CL-dark (e.g. grains 6, 7, 8, 9 and 10 in Fig. 3a). In grains displaying both domains, the CL-dark rim consistently overgrows the CL-grey zone (e.g. grains 1, 4, 5, 12, 13, and 14 in Fig. 3a). Both domains are present in all samples but the occurrence of both in single grains is especially well-developed in sample EOMP-01, a muscovite-biotite quartz monzogranite. Grains from La Palmerita granitoid exhibit simpler textures than those from the Marcabelí pluton. The most common feature is a parallel/oscillatory/patchy core surrounded and cut by a distinct CL-grey or dark rim showing oscillation (Fig. 3b).

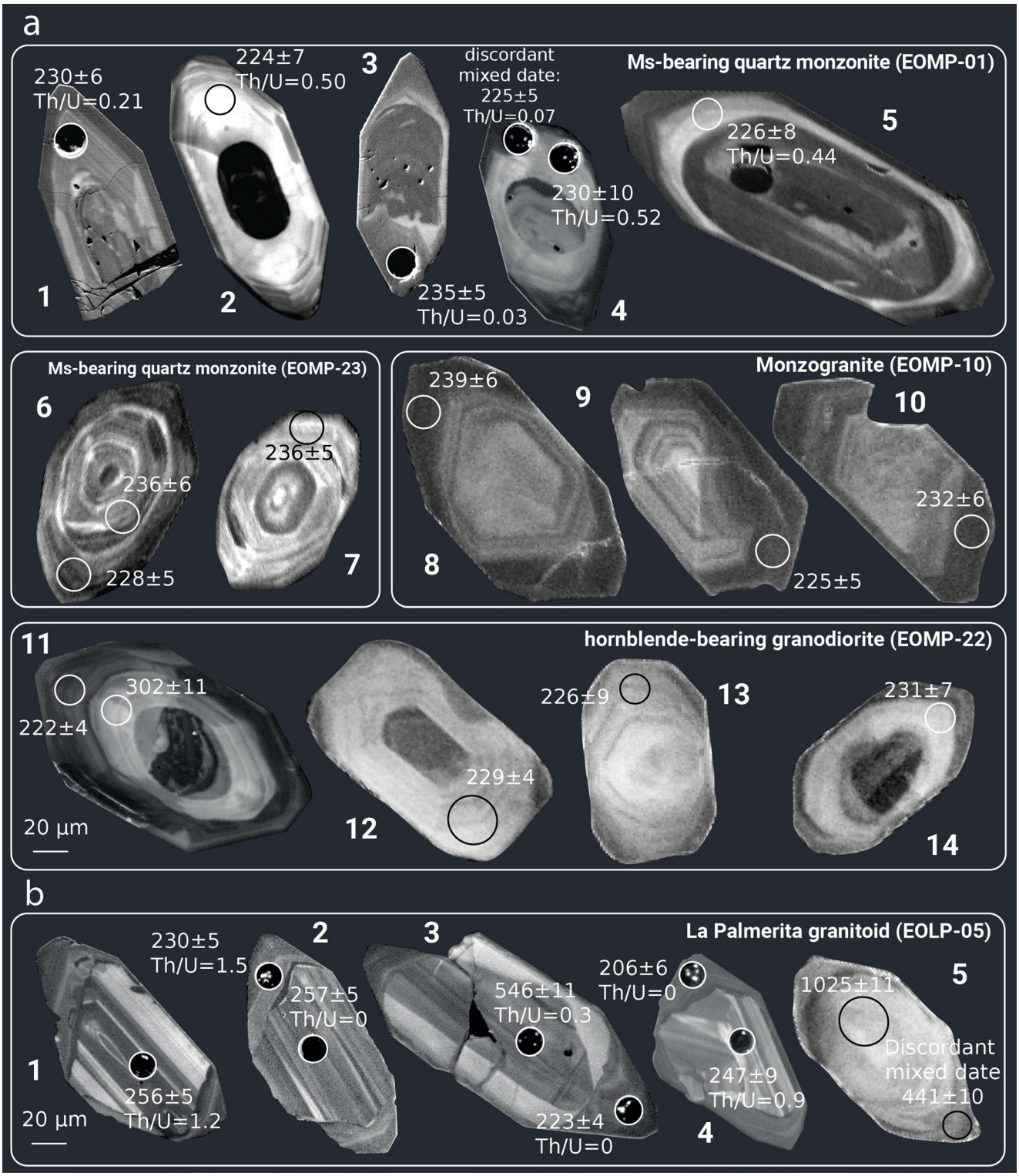


Fig. 3 Representative zircon cathodoluminescence (CL) and charge contrast images of the igneous samples of the Marcabelí pluton (**a**) and La Palmerita granitoid (**b**). Zircons on all samples show multiple generations of inherited cores and rims. Zircons from La Palmerita sometimes present cores with dates younger than 270 Ma, overgrown by a CL-grey rim

U–Pb and trace element zircon data

A total of 713 analyses were conducted on the four different samples from the Marcabelí pluton, from which 514 are concordant and younger than 270 Ma. These comprise 338 with a 16 µm spot size and 176 with a 30 µm spot size. Regarding the granitoid sample from La Palmerita, 195 analyses were performed. Following the filtering process, 30 analyses were retained, comprising 28 with a 16 µm spot size and 2 with a 30 µm spot size. This high number of filtered analyses is attributed to the presence of thin rims, from which mixed analyses produced discordant ages, and a high portion of old inherited cores (i.e. grain 5 on Fig. 3b). The Tera-Wasserburg diagrams of the concordant dates of each granitoid sample are reported in the supplementary material (Fig. S3).

The results of the $^{206}Pb/^{238}U$ dates are presented as rank-order plots for the four samples of the Marcabelí pluton in Fig. 4a. Kernel density estimates (KDEs) are also present in the supplementary material (Fig. S5). The combined results for these four samples, as well as the results for the granitoid sample from La Palmerita, are presented in Fig. 4b and c, respectively. Zircons from the muscovite-biotite quartz monzonite (EOMP-01) are divided into two populations based on their Th/U ratios, CL imaging, and trace-element patterns; see below for more details. The weighted means calculated for this sample from the Marcabelí pluton are 230.4 ± 0.8/2.8 (MSWD = 2.8, n = 107) and 226.4 ± 1.3/2.8 (MSWD = 5.0, n = 59) Ma for Th/U ratio > and < 0.1, respectively. The other muscovite-bearing quartz monzonite (EOMP-23) yields a weighted mean of 230.1 ± 1.3/2.9 Ma (MSWD = 3.1, n = 52). The weighted mean for the monzogranite (EOMP-10) is 227.1 ± 1.2/2.8 (MSWD = 6.5, n = 68) and is 228.8 ± 0.6/2.6 (MSWD = 3.2, n = 140) Ma for the hornblende-bearing granodiorite (EOMP-22). The weighted mean of the sample of La Palmerita granitoid (EOLP-05) is 232.0 ± 2.2/3.4 (MSWD = 6.3, n = 24) Ma. Overall, the weighted means of the five samples are within uncertainty of each other and exhibit high MSWD values, which are not compatible with a simple single age for each sample.

Temperature estimates were obtained with Ti-in-zircon thermometry using the calibration of Ferry and Watson (2007). For Ti-in-zircon thermometry, a_{SiO_2} was fixed to 1 for all the samples due to the presence of quartz. Ti-bearing phases were not directly observed in samples EOMP-01, EOMP-10, and EOMP-22. However, because ilmenite is present in other samples of the Marcabelí granite and is a common accessory mineral in S-type granites (e.g. Schiller and Finger 2019), a_{TiO_2} value of 0.5 was assumed for these samples. Because titanite was found in EOMP-23 and ilmenite in EOLP-05, a_{TiO_2} was fixed to 0.4 and 0.5, respectively (Schiller and Finger 2019). Results are shown in Fig. 5. In addition, chondrite-normalised zircon REE patterns (REE_N) are shown in Fig. 6. All samples show a pronounced negative Eu anomaly (Eu*) and positive Ce anomaly (Ce*), and a significant enrichment in HREEs relative to MREEs and LREEs. The sample EOMP-01 shows two populations: one with Th/U > 0.1 and slight LREE–MREE enrichment, and another with Th/U < 0.1 and relative LREE–MREE depletion. In addition, the temperature estimates for this sample show an important degree of variability: between 700 and 920 °C for zircon analyses with Th/U ratios > 0.1, and between 550 and 670 °C for analyses with Th/U ratios < 0.1. Sample EOMP-23 also shows a similar trend in temperature and trace elements to EOMP-01, but with a less pronounced difference between the two groups. The two samples EOMP-10 and EOMP-22 of the Marcabelí pluton show relatively uniform REE_N and Ti-in-zircon temperature across the zircon analyses. The temperature estimates range mostly between 650 and 850 °C, while the Th/U ratios are comprised between 0.2 and 0.5. Overall, a positive trend between Ti content and Th/U ratios is observed across all samples.

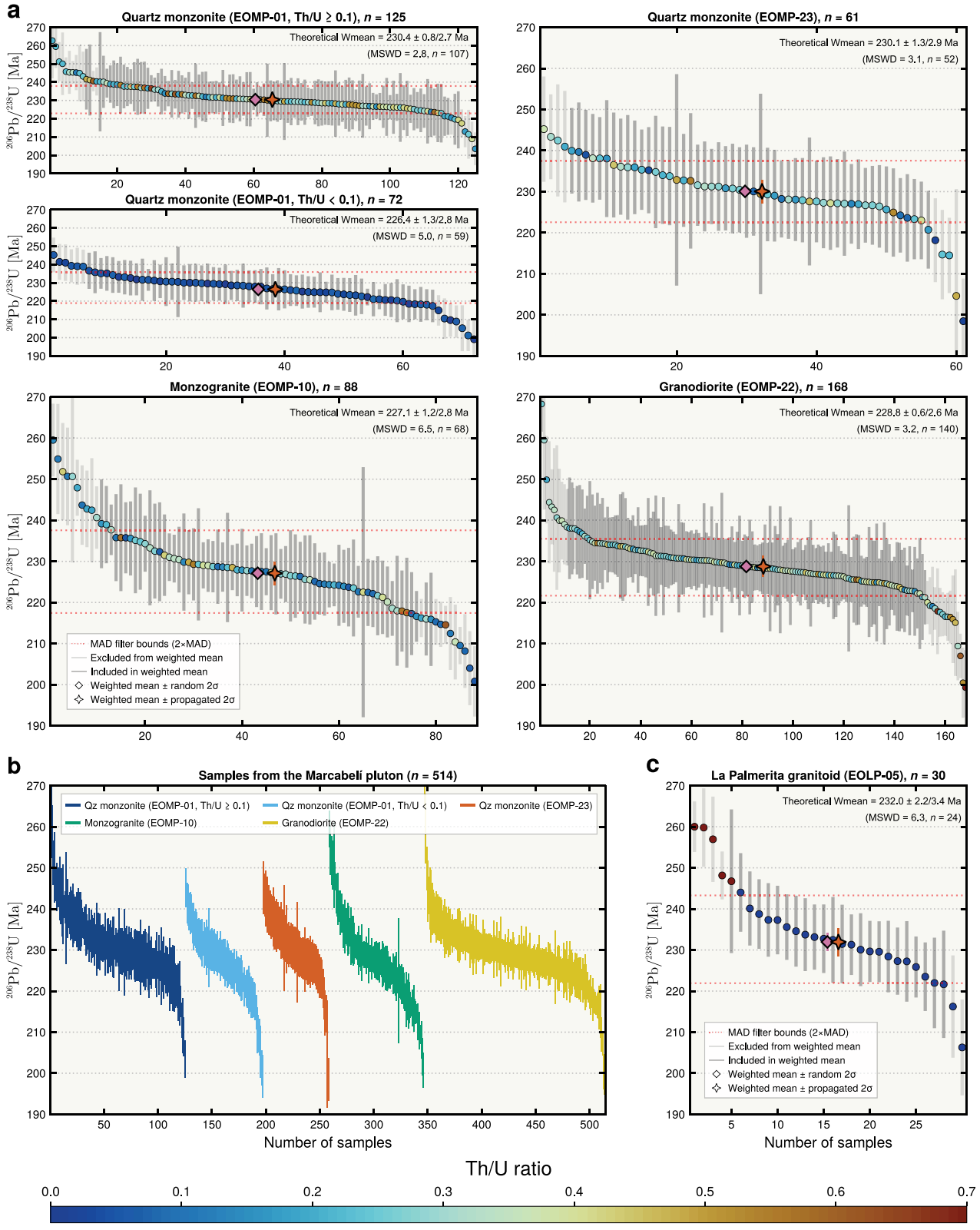
The zircons from La Palmerita granitoid (EOLP-05) are characterised by Th/U ratios below 0.1, a similar general trend for REE_N and temperature estimates between 580 and 680 °C (Figs. 5b and 6b). Five analyses deviate from this trend, with enrichment in LREEs and MREEs, particularly Ce, a smaller Eu*, and a Th/U ratio of approximately 0.7 to 1.5. The Ti-in-zircon temperature also records up to 800 °C, and $^{206}Pb/^{238}U$ dates are older than ca. 235 Ma, making them significantly older than the rest of the analyses (Fig. 5b). These analyses correspond to different CL domains and are cores in the zircons (i.e. Figure 3b grains 1, 2 and 3).

Fig. 4 Rank-order plot of the $^{206}Pb/^{238}U$ dates for the igneous samples between 270 and 190 Ma. **a** Four samples from the Marcabelí pluton. Sample EOMP-01 is separated in two groups based on Th/U ratio. **b** Comparison of all the samples from the Marcabelí pluton. **c** Sample from La Palmerita granitoid. The red dotted lines represent the acceptable range at 1σ for the analyses to be included in the weighted mean calculation. These intervals are computed using the median absolute deviation method (MAD). Each weighted mean is reported with two uncertainties accounting for the contribution of random and systematic uncertainties (see Analytical methods part for more details). All uncertainties are reported at 2σ

Migmatites from La Bocana

Zircon morphology

Zircon grains in the three groups of migmatitic samples from La Bocana are similar in size and shape, mostly subrounded or euhedral. Their lengths range from 40 to 300 µm, and their widths from 20 to 180 µm. The aspect ratios are ~1.5–5. Noticeable differences and characteristics in CL


a
Quartz monzonite (EOMP-01, Th/U ≥ 0.1), n = 125
Theoretical Wmean = 230.4 ± 0.8/2.7 Ma
(MSWD = 2.8, n = 107)
Quartz monzonite (EOMP-01, Th/U < 0.1), n = 72
Theoretical Wmean = 226.4 ± 1.3/2.8 Ma
(MSWD = 5.0, n = 59)
Quartz monzonite (EOMP-23), n = 61
Theoretical Wmean = 230.1 ± 1.3/2.9 Ma
(MSWD = 3.1, n = 52)
Monzogranite (EOMP-10), n = 88
Theoretical Wmean = 227.1 ± 1.2/2.8 Ma
(MSWD = 6.5, n = 68)
Granodiorite (EOMP-22), n = 168
Theoretical Wmean = 228.8 ± 0.6/2.6 Ma
(MSWD = 3.2, n = 140)
MAD filter bounds (2×MAD)
Excluded from weighted mean
Included in weighted mean
Weighted mean ± random 2σ
Weighted mean ± propagated 2σ
206Pb/238U [Ma]
b
Samples from the Marcabelí pluton (n = 514)
Qz monzonite (EOMP-01, Th/U ≥ 0.1)
Qz monzonite (EOMP-01, Th/U < 0.1)
Qz monzonite (EOMP-23)
Monzogranite (EOMP-10)
Granodiorite (EOMP-22)
Number of samples
c
La Palmerita granitoid (EOLP-05), n = 30
Theoretical Wmean = 232.0 ± 2.2/3.4 Ma
(MSWD = 6.3, n = 24)
Number of samples
Th/U ratio

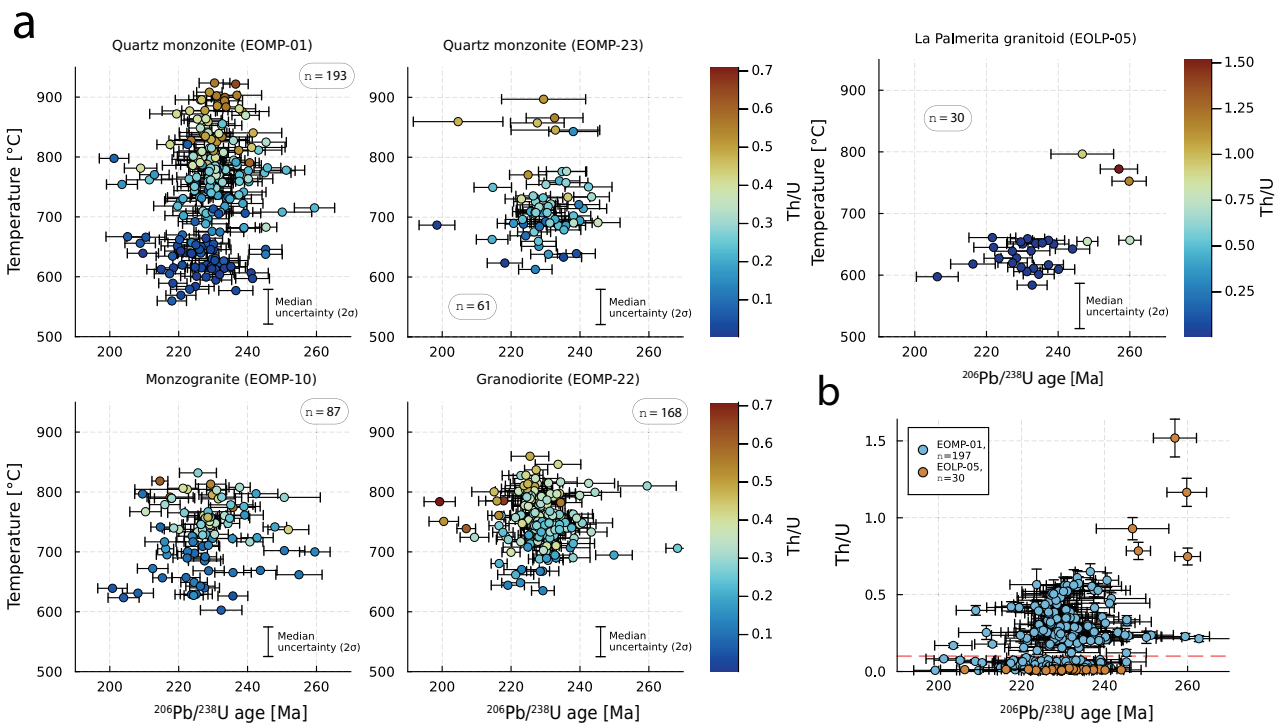


Fig. 5 **a** Ti-in-zircon thermometry vs. $^{206}Pb/^{238}U$ dates from the zircon analyses of the igneous samples calculated using the formulation of Ferry and Watson (2007). The activities are assumed to be a_{SiO_2} = 1 and a_{TiO_2} = 0.5 for all samples except EOMP-23 where a_{TiO_2} was fixed to 0.4 due to the presence of Ttn in the sample. The colour bar represents the Th/U ratio. The median uncertainty for the temperature estimate is calculated by propagating the uncertainties from the Ti analyses. **b** Th/U ratio vs. $^{206}Pb/^{238}U$ dates for the sample of the Marcabelí pluton showing the most variability, and the sample of La Palmerita granitoid. The red horizontal dashed line represents the value of Th/U ratio equal to 0.1. All uncertainties are reported at 2σ

images are observed between the three different groups of samples (Fig. 7). Zircons from the Upper La Bocana unit (EOLB-53, EOLB-55, EOLB08, EOLB-10) often show a CL-dark homogeneous rims around bright cores (Fig. 7a and b), whereas zircons from the Lower La Bocana unit (EOLB-04, EOLB-37 in Fig. 7c) exhibit thicker brighter rims (on the order of 30 µm compared to 10 to 20 µm for Upper La Bocana zircons) with common oscillatory zoning and sometimes multiple rims (oscillatory to homogeneous, bright-Cl to gray-CL responses) recording similar dates. Zircons from the migmatites in Upper La Bocana preserve an important proportion of bright cores with dates < 270 Ma, which range mostly between ca. 240 and 270 Ma for the diatexites (EOLB-53 and EOLB-55) and between ca. 220 and 235 Ma for the leucosomes of the stromatic metatexites (EOLB-08 and EOLB-10).

U–Pb and trace element zircon data

The total number of analyses for all the migmatitic samples from the La Bocana unit is 697, from which 338 were discarded due to discordance or dates older than 270 Ma. This represents filtering of 88 analyses for both samples of diatexite from the Upper La Bocana unit (EOLB-53 and EOLB-55), 90 for both samples of the leucosomes from metatexites (EOLB-08 and EOLB-10), and 181 for the diatexite samples of the Lower La Bocana unit (EOLB-04 and EOLB-37). The Tera-Wasserburg diagrams of the concordant dates of each migmatitic sample are reported in the supplementary material (Fig. S3). The results of the $^{206}Pb/^{238}U$ dates are shown as KDEs for the six samples of migmatites in Fig. 8. Chondrite-normalised zircon REE diagrams for the two samples of diatexite in Upper La Bocana are reported in Fig. 9, and REE_N of the samples from the metatexites in Upper La Bocana and the diatexites from Lower La Bocana are shown in Fig. 10. The results of Ti-in-zircon thermometry using the calibration from Ferry and Watson (2007) are shown in Fig. 11 for the six samples. For Ti-in-zircon thermometry, a_{SiO_2} was fixed to unity due to the presence of quartz and a_{TiO_2} was assumed to be 0.5 for the samples in the Upper La Bocana unit and 1 for the Lower La Bocana unit, due to the presence of ilmenite and coexistence of ilmenite and rutile in the samples, respectively.

Two distinct zircon populations can be defined in the diatexite samples from the Upper La Bocana unit (EOLB-53 and EOLB-55) based on their $\ln(Ce_N)/\ln(Lu_N)$ ratios (Fig. 9a).

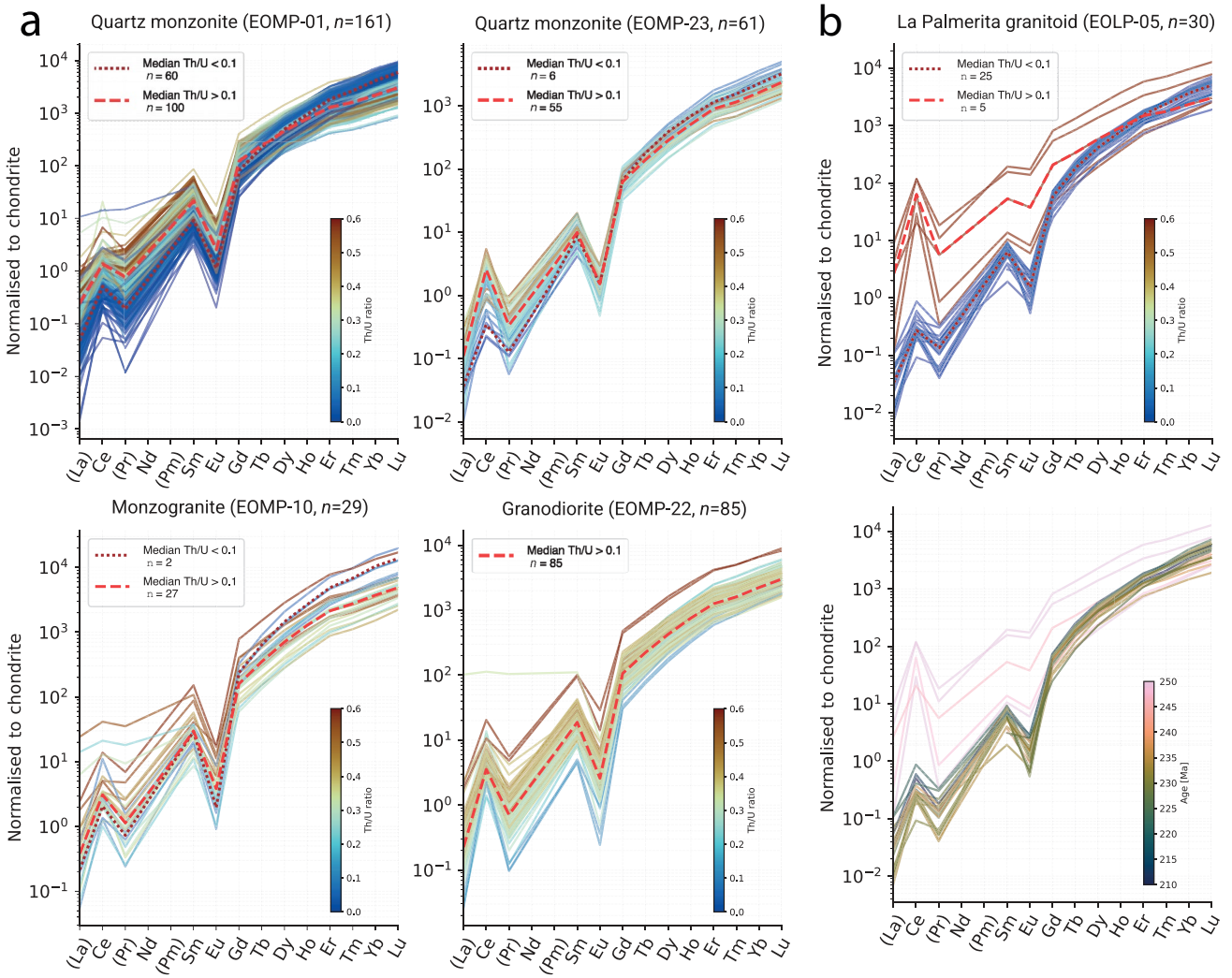


Fig. 6 Chondrite-normalised REE diagrams of the zircon analyses from the igneous samples. **a** Four samples of the Marcabelí pluton. **b** Sample from La Palmerita granitoid. The dark and light red dashed lines represent the median calculated for analyses below and above 0.1 Th/U ratio, respectively, and the colours represent either Th/U ratio or the $^{206}Pb/^{238}U$ dates. The values of La, Pr and Pm were not measured and are estimated by extrapolation from the slope of Nd–Sm. These elements are indicated in brackets. Chondrite values are from McDonough and Sun (1995)

These ratios are used as a proxy for Ce* due to the absence of La and Pr measurements. These populations also differ in CL characteristics: the older group exhibits CL-bright, oscillatory-zoned cores, whereas the younger group shows CL-dark rims (e.g. grains 2 and 4 in Fig. 7a). Other distinctions include Th/U ratios and Ti-in-zircon temperature: the older population has Th/U ratios greater than 1 and temperatures between 750 and 850 °C, while the younger population has Th/U ratios less than 1 and temperatures between 600 and 750 °C (Figs. 8a and 12a). A total of 88 analyses yielded weighted means of 248.2 ± 5.5/6.1 Ma (MSWD = 15.3, n = 9) and 250.1 ± 3.2/4.2 Ma (MSWD = 14.7, n = 23) for the older population and 227.0 ± 1.8/3.1 Ma (MSWD = 4.3, n = 20) and 231.0 ± 2.4/3.6 Ma (MSWD = 6.6, n = 20) for the younger population in EOLB-53 and EOLB-55, respectively. The large MSWD values in the older populations (15.3 and 14.7) do not allow the interpretation of these weighted means as geological ages, given the data dispersion.

Two distinct zircon populations are also present in the metatexite samples (EOLB-08 and EOLB-10). One population shows relative enrichment in LREEs and MREEs but depletion in HREEs, and is associated with higher Th/U values and CL-bright domains in CL imaging (Fig. 10a). Using a Th/U value of 0.1 as the threshold, analyses with Th/U > 0.1 represent 15% and 44% of the analyses in EOLB-08 and EOLB-10, respectively. This distinction also correlates with Ti-in-zircon temperature estimates: analyses with Th/U > 0.1 yield temperatures between ~750 and 900 °C, while those with Th/U < 0.1 fall between ~550 and 700 °C (Fig. 11b). Despite these geochemical differences,

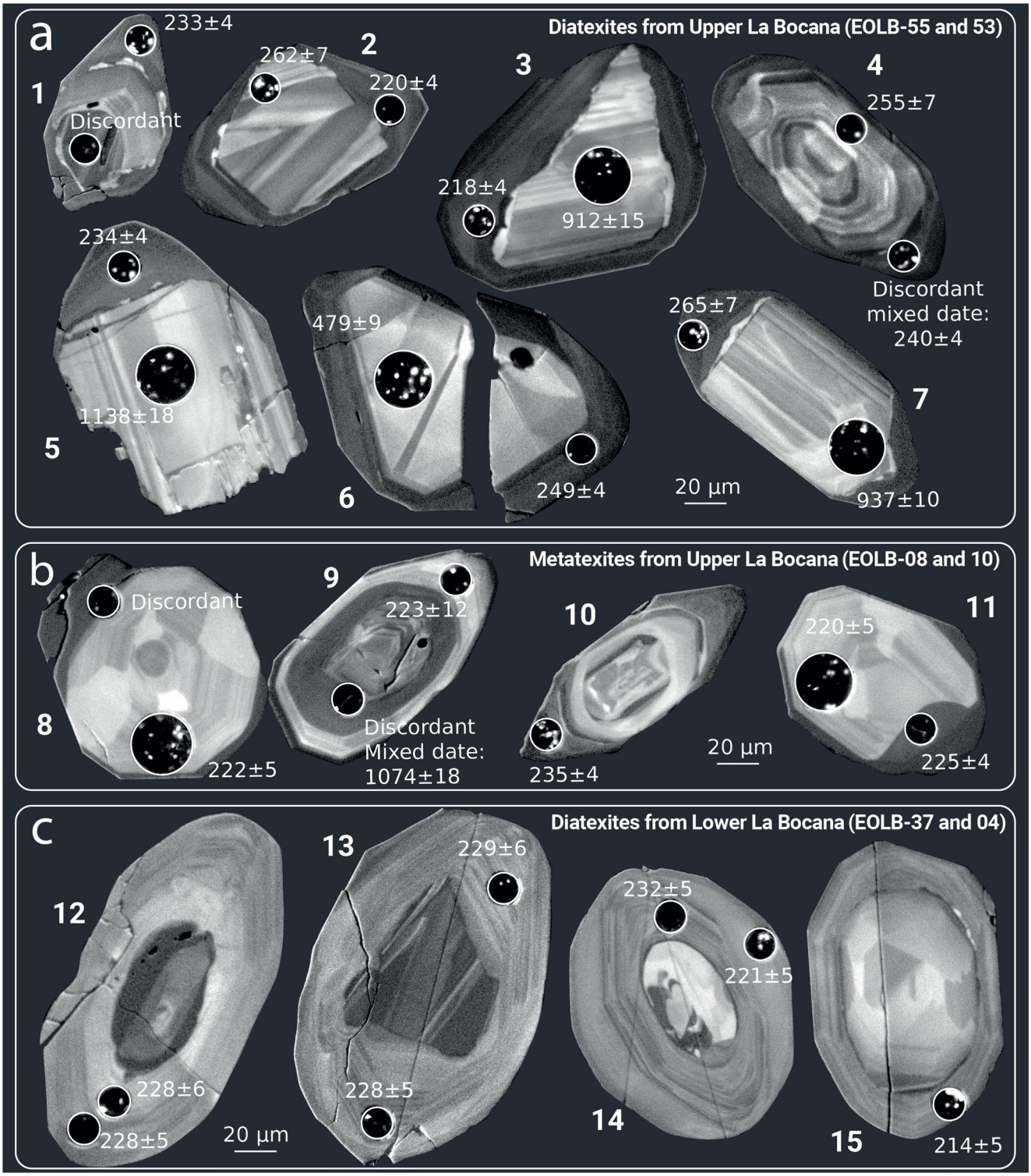


Fig. 7 Representative zircon cathodoluminescence (CL) of the two samples of diatexites in Upper La Bocana (EOLB-53, EOLB-55) (**a**), of leucosomes in metatexites in Upper La Bocana (EOLB-08, EOLB-10) (**b**), and of diatexites in Lower La Bocana (EOLB-04, EOLB-37) (**c**) with $^{206}Pb/^{238}U$ dates from LA-ICP-MS analyses. Zircons on all samples often show multiple generations of inherited cores. Zircons in (**a**) present CL-bright cores with dates ca. 240–260 Ma, overgrown by thin CL-dark rims with ages ranging from ca. 220–240 Ma. Zircons in (**b**) show CL-bright cores with thin CL-dark rims with the same date within uncertainty, ranging from ca. 220–240 Ma. Zircons in (**c**) have large CL-grey rims showing often oscillatory zoning with dates between ca. 220–240 Ma. Young CL-bright cores and CL-dark rims correlate with Th/U ratios and temperature estimates for (**a**) and (**b**), see Fig. 12

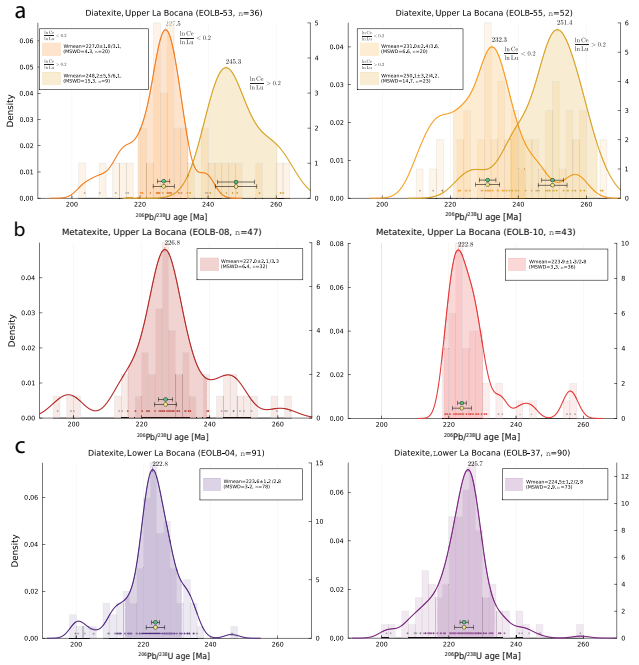


Fig. 8 Kernel density estimates and histograms of the $^{206}Pb/^{238}U$ dates of the migmatitic samples. **a** Two samples from diatexites in Upper La Bocana. **b** Two samples from leucosomes in metatexites in Upper La Bocana. **c** Two samples from diatexites in Lower La Bocana. The coloured areas represent the acceptable range at 1σ for the analyses to be included in the weighted mean calculation. These intervals are computed using the median absolute deviation method. The coloured dots represent the analyses included in that range. The ages are reported with two uncertainties at 2σ: without systematic uncertainty propagation, and with systematic uncertainty. Two populations are distinguished in (**a**), based on $\ln(Ce_N/Lu_N)$ ratios. This also correlates with CL textures, Th/U ratios and temperature estimates (see Figs. 10 and 12)

both populations yield overlapping dates within uncertainty, and are therefore combined to obtain weighted mean ages of 227.0±2.1/3.3 Ma (MSWD=6.4, n=32) for EOLB-08 and 223.9±1.3/2.8 Ma (MSWD=3.3, n=36) for EOLB-10 (Fig. 8).

In contrast, the Lower La Bocana samples (EOLB-04 and EOLB-37) display relatively homogeneous LREE and MREE contents, but a broader range in HREE content, as reflected in their $\ln(Gd_N)/\ln(Lu_N)$ values. Combined, 83 out of 180 analyses of both samples yield ratios below 0.6 (Fig. 10b). This is used as a proxy for flat HREE profile, which is commonly interpreted as reflecting zircon growth concurrent with or following garnet growth (e.g. Kohn and Kelly, 2018). This correlates well with Ti-in-zircon temperature estimates for the sample EOLB-04, with more flat HREE corresponding to higher temperatures, but not for sample EOLB-37, where the highest temperature estimates correspond to intermediate values of $\ln(Gd_N)/\ln(Lu_N)$ (Fig. 10b). Furthermore, this chemical distinction does not result in clear differences in Th/U or dates for both samples: they define a single population with Th/U<0.1 and no clear correlation with HREE and dates (Figs. 11c, S7). Consequently, single weighted mean ages of 223.6±1.2/2.8 Ma (MSWD=3.2, n=78) for EOLB-04 and 224.5±1.2/2.8 Ma (MSWD=2.9, n=73) for EOLB-37 were computed (Fig. 8c).

Metagabbro from Piedras

Titanite morphology

The selected titanite grains are mostly transparent and slightly yellow, with irregular, rounded shapes. Their sizes range from 300 µm to 500 µm. The grains are homogeneous in composition, with no observed sector zoning on back-scattered images (BSE). Locally, zircon or rutile inclusions are observed (Fig. 12c).

U–Pb and trace element titanite data

Ninety four analyses yield an isochron age at 227.5±4.5 (n=94) Ma from an upper-intercept unconstrained regression with a dispersion of 0.6±0.2 Ma (Fig. 12a). Zr-in-titanite temperature estimates using the calibration of Hayden et al. (2008) show temperature ranging mostly between 710 and 750 °C assuming a pressure of 0.8 GPa from a depth of around 25 km (based on the mapped structural level in the studied section). The activities a_{SiO_2}, a_{TiO_2}, and a_{Zr} are set to unity due to the presence of quartz, rutile, and zircon in the sample (Fig. 12b).

Discussion

Interpretation of zircon U–Pb and trace element data

The calculation and interpretation of zircon U–Pb ages from S-type granitoids and migmatitic systems is challenging. Geological specificities, such as the high degree of inheritance increasing the risk of analytical mixing of different age zones during ablation of the grains (Gulson and Krogh 1973; Paterson et al. 1992), and the potentially long-lived nature of melting and (re)crystallisation processes (Miller et al. 2007; Gordon et al. 2008; Sparks et al. 2019; Van Zalinge et al. 2022) need to be accounted for. Additionally, common issues with the U–Pb system in zircons, such as Pb-loss, must be considered. In particular, concealed Pb loss is problematic: analyses may appear falsely concordant because analytical uncertainties in $^{206}Pb/^{238}U$ and $^{207}Pb/^{235}U$ are positively correlated, causing the resulting trend to align with the Concordia line (e.g. Andersen et al. 2019). In addition

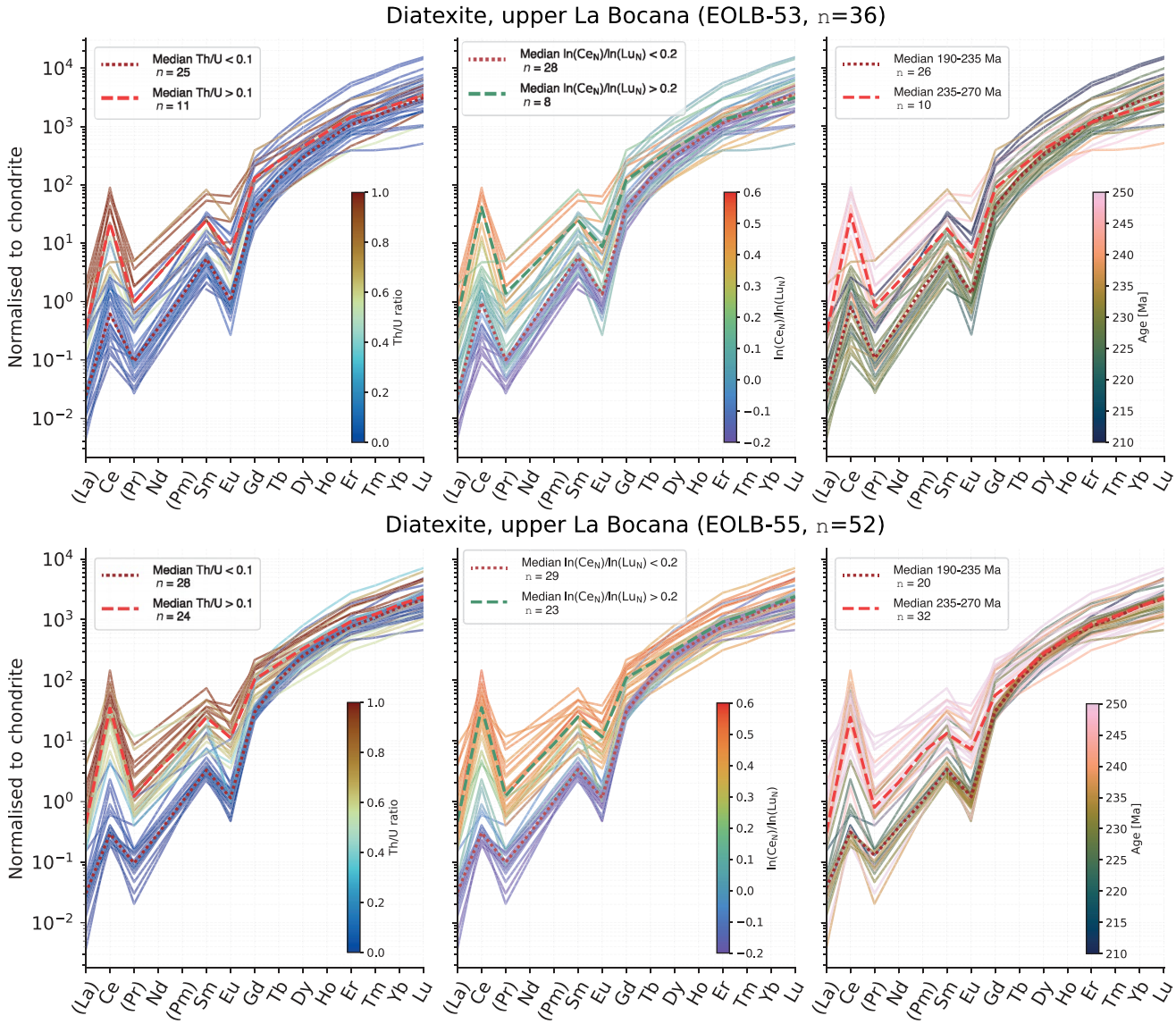


Fig. 9 Chondrite-normalised REE diagrams of the samples of diatexites from Upper La Bocana: EOLB-53 at the top and EOLB-55 at the bottom. Two populations of zircon across both samples show distinguishable REE_N patterns, which correlate with Th/U, $ln(Ce_N/Lu_N)$ ratios and $^{206}Pb/^{238}U$ dates. The values of La, Pr and Pm were not measured and are estimated by extrapolation from the slope of Nd–Sm. These elements are indicated in brackets. Chondrite values are from McDonough and Sun (1995)

to diffusion-related mechanisms, melt-mediated coupled dissolution-precipitation replacement reactions can also produce near-concordant Pb-loss arrays through variable redistribution and loss of radiogenic Pb at the reaction interface (Asimus et al. 2024; Daczko et al. 2024). When calculating weighted mean ages from individual zircon analyses of a single event, it is possible to interpret the statistical dispersion in the dates as a combination of these processes (see Fig. S8). Some of these processes mainly contribute to decreasing (e.g. Pb-loss) or increasing (e.g. mixing with inherited cores) the date of individual analyses, hindering interpretation by adding non-informative dispersion relative to the geological processes of interest. On the other hand, some of these processes convey meaningful information, which can be termed as geological dispersion, such as protracted zircon growth and recrystallization (Taylor et al. 2016; Kunz et al. 2018; Tedeschi et al. 2018). Estimating the contributions of analytical and geological dispersion is nontrivial. There is increasing evidence that the geological dispersion in magmatic systems is beyond instrumental uncertainties and that it cannot be attributed to Pb-loss or inheritance alone, in particular using TIMS or SIMS (e.g. Miller et al. 2007; Schmitt et al. 2023; Szymanowski et al. 2019). Based on this, the scatter in dates exceeding the analytical uncertainty observed in the granitic and migmatitic

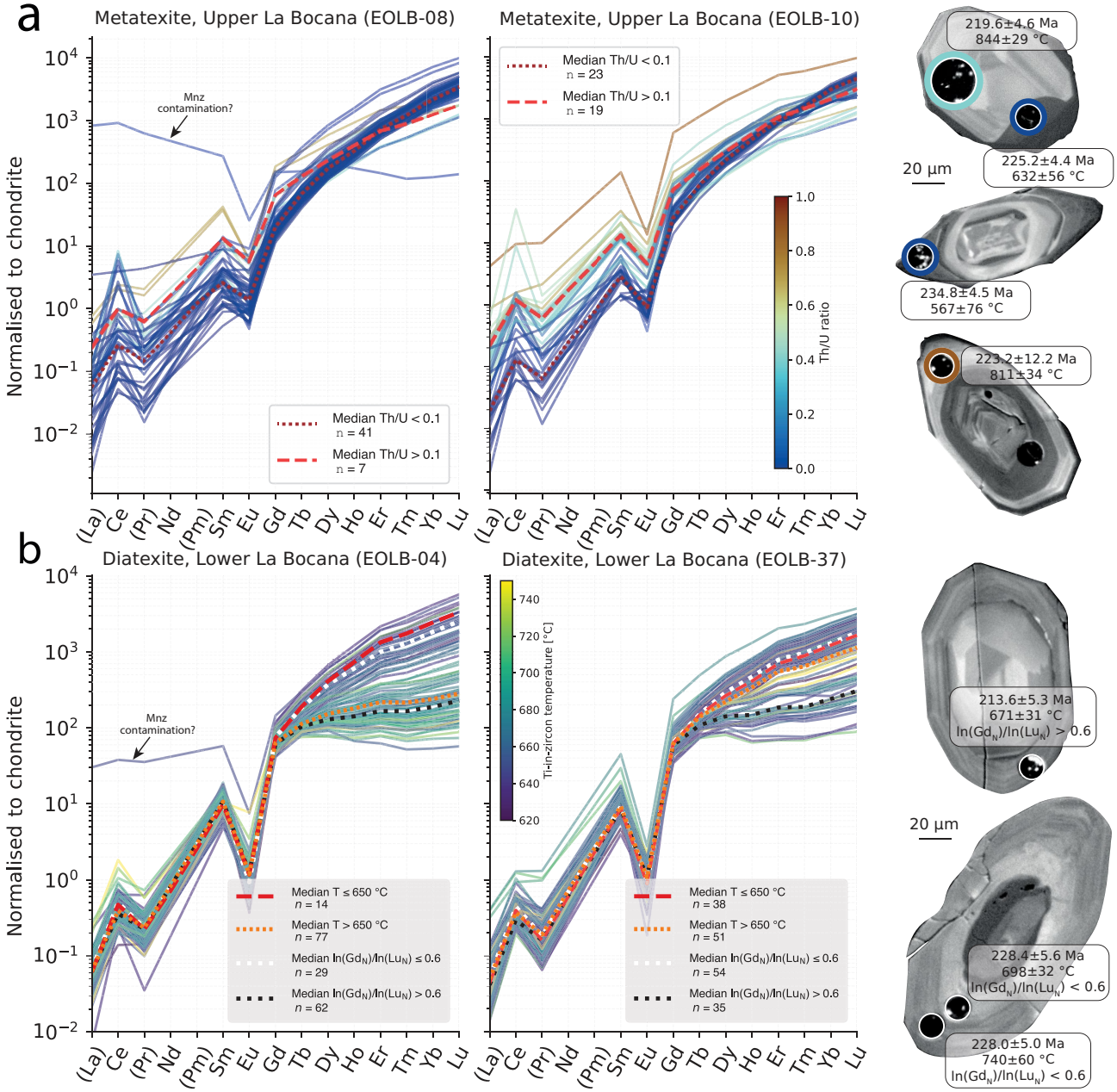


Fig. 10 Chondrite-normalised REE diagrams of the zircon analyses and corresponding representative CL imaging from the leucosomes of metatexites from Upper La Bocana (**a**) and from diatexites in Lower La Bocana (**b**). (**a**) shows correlation between REE_N, Th/U ratio, temperature estimates and dark and bright CL domains. (**b**) shows depletion in the $HREE_N$ across the samples with correlation with temperature estimates for EOLB-04 but no clear pattern for EOLB-37, and no corresponding systematic in CL imaging, dates and temperature estimates. The values of La, Pr and Pm were not measured and are estimated by extrapolation from the slope of Nd–Sm. These elements are indicated in brackets. Colours in the CL images correspond to the value of Th/U for the Upper La Bocana sample. Chondrite values are from McDonough and Sun (1995)

samples can be interpreted as containing meaningful geological information.

By spatially integrating these data with trace-element analyses, zircon populations can be discriminated based on their geochemical signatures, thereby offering additional constraints on crystallisation conditions and improving geological understanding. In particular, REEs have been used to infer the influence of other minerals during zircon growth, such as HREE depletion due to garnet (Rubatto 2002), LREE depletion due to monazite (e.g. Rubatto et al. 2009) or the negative Eu* linked to feldspar (Hinton and Upton 1991; Schaltegger et al. 1999). Negative Eu* in

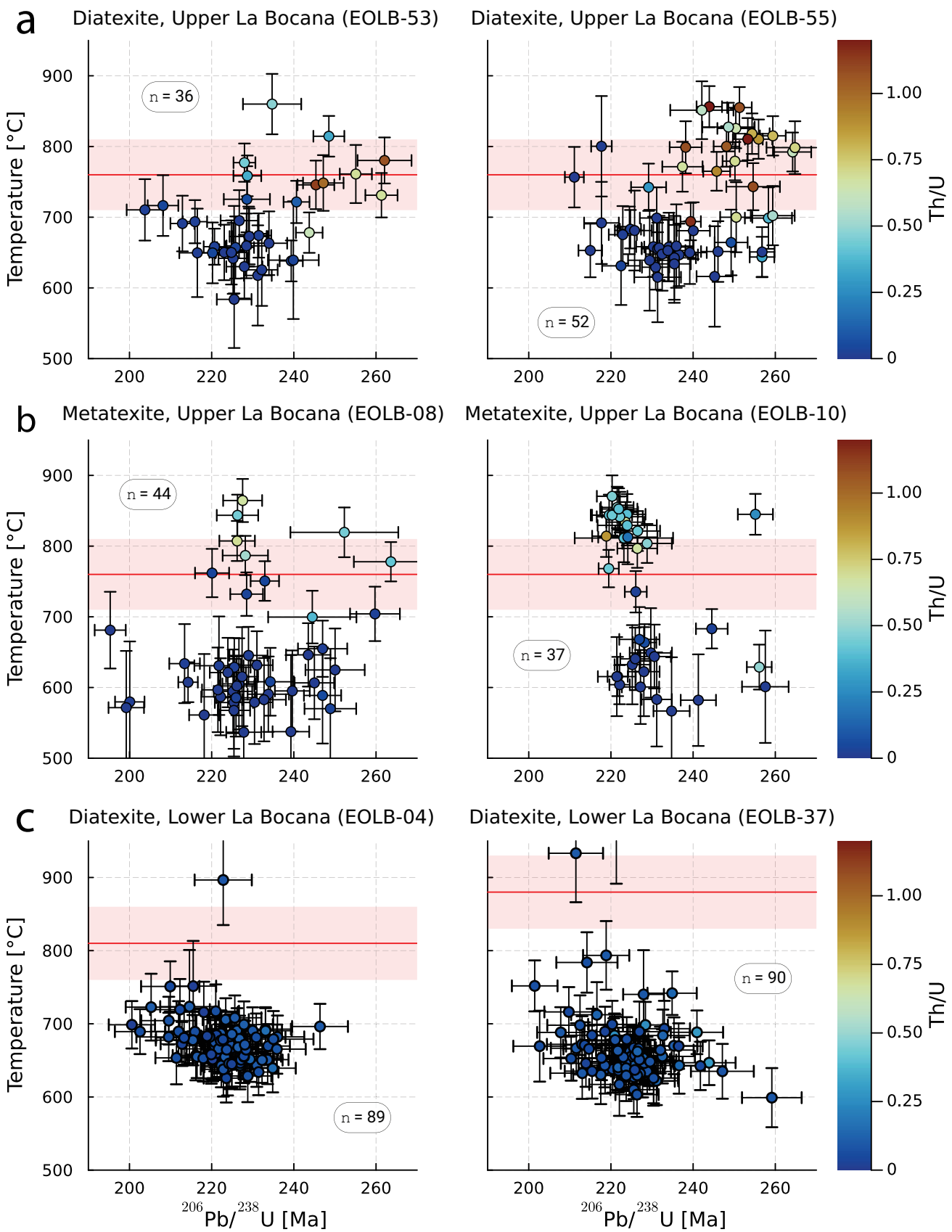

a
Diatexite, Upper La Bocana (EOLB-53)
Diatexite, Upper La Bocana (EOLB-55)
n = 36
n = 52
b
Metatexite, Upper La Bocana (EOLB-08)
Metatexite, Upper La Bocana (EOLB-10)
n = 44
n = 37
c
Diatexite, Lower La Bocana (EOLB-04)
Diatexite, Lower La Bocana (EOLB-37)
n = 89
n = 90
Temperature [°C]
500
600
700
800
900
200
220
240
260
206Pb/238U [Ma]
Th/U
0
0.25
0.50
0.75
1.00

Fig. 11 Ti-in-zircon thermometry vs. $^{206}Pb/^{238}U$ dates from the zircon analyses of the migmatitic samples calculated using the formulation of Ferry and Watson (2007). **a** Two samples from diatexites in Upper La Bocana. **b** Two samples from leucosomes in metatexites in Upper La Bocana. **c** Two samples from diatexites in Lower La Bocana. The activities are assumed to be $a_{SiO_2} = 1$ for all samples and $a_{TiO_2} = 0.5$ for (**a**) and (**b**) and 1 for (**c**) due to the presence ilmenite and rutile in the samples, respectively. The colour bar represents the Th/U ratio. The uncertainties for the temperature estimate are calculated by propagating the uncertainties from the Ti analyses. The red lines indicate the maximum metamorphic temperature estimates from Riel et al. (2013) and Riel et al. (2016) for samples geographically closest to the samples used in this study. The red box gives the associated uncertainty of 50 °C on the temperature estimates. All uncertainties are reported at 2σ

conjunction with the positive Ce* has also been used to infer the redox state of the magma from which zircon is crystallising, as Eu^{2+} and Ce^{4+} are incompatible or preferably incorporated in the Zr^{4+} site, respectively (e.g. Murali et al. 1983; Ballard et al. 2002; Trail et al. 2012). The Th/U ratio has also been used extensively to distinguish between magmatic (Th/U > 0.1) and metamorphic zircons (Th/U < 0.1) (e.g. Rubatto 2017). It is linked to multiple factors, such as the presence of minerals with high or low Th/U ratios, (e.g. monazite, titanite, allanite, apatite or xenotime), equilibrium vs. disequilibrium behaviour, open-system behaviour or aqueous fluid interaction (e.g. Rubatto 2017; Yakymchuk et al. 2018). In the case of metapelitic migmatites, coeval growth of monazite during cooling, which preferentially incorporates Th, is the common interpretation for low Th/U values. This distinction between magmatic and metamorphic rocks presents limitations with S-type granitoids, as their source is metasediments, which may inherently have low Th/U ratios (e.g. Roberts et al. 2024), but it is mostly valid for metapelitic migmatites, except at UHT. Another trace element of interest in zircon is Ti, which is used as a thermometer in Ti-in-zircon temperature estimates (e.g. Ferry and Watson 2007).

The validity of coupling Ti-in-zircon thermometry, REE patterns, and $^{206}Pb/^{238}U$ dates relies on these systems remaining closed throughout the post-peak cooling history of the sequence. Titanium diffusion in zircon is negligible below 800 °C (Bloch et al. 2022), and maximum recorded temperatures of ca. 850–900 °C (Figs. 5a and 11a and b) suggest a Ti closure temperature around 900 °C for this sequence. This is further supported by large zircon grain sizes (200–300 µm), which favour higher closure temperatures and imply rapid cooling. The REE and Pb systems are even more retentive, with closure temperatures estimated above 1000 °C and 900 °C respectively (Cherniak et al. 1997; Cherniak and Watson 2001; Cherniak 2010). Together, these constraints indicate that all three systems were effectively closed during the metamorphic evolution recorded here, supporting their combined interpretation. Temperature estimates approaching 900 °C should nonetheless be treated with caution, as they may reflect cooling rather than peak conditions. Additionally, metamictisation, the progressive radiation damage to the zircon lattice driven by alpha-decay recoil from U and Th, can compromise Pb retention and distort trace-element patterns, leading to discordant U–Pb analyses, elevated common Pb, and anomalous REE signatures. In this study, grains were screened for evidence of metamictisation using CL imagery, U–Pb discordance, common Pb levels, and anomalous trace-element patterns, and no significant metamictisation was identified in the analysed population. An alternative approach to detect metamictisation is using Raman spectroscopy, which was not performed in this study but could be included in future works (Nasdala et al. 2001, 2003). Furthermore, no porosity or microstructures indicating dissolution-precipitation in the zircons were observed. Finally, only concordant data at 2σ were kept in this study in order to limit potential lead-loss influence.

Emplacement of granitoids in the El Oro complex

The rank-order plots of the granitoid samples show widespread $^{206}Pb/^{238}U$ dates, ranging over ca. 20 Myr (Fig. 4). The sample of muscovite-bearing quartz monzonite EOMP-01 shows the greatest variability, with two populations based on CL images and trace element data (Fig. 3a). Although there is an overlap in age between the two populations, the youngest is interpreted to represent the final stage of crystallisation of zircon grains, based on the lowest temperature estimates recorded, between ~580 and 680 °C, and Th/U ratios < 0.1. The older population, showing mostly oscillatory zoning, is interpreted to have crystallised at a higher temperature, with a higher melt fraction, based on higher temperature estimates of ~700–900 °C and Th/U ratios > 0.1. Ti-in-zircon temperature estimates below the wet solidus (i.e. 680 °C, Fig. 5) are most likely the result of low Ti contents in the final vestiges of melt during zircon crystallisation, or as a result of poor equilibrium between the zircon and surrounding melts in the final cooling stages. Therefore, we propose that they reflect Ti-unbuffered conditions during cooling of the pluton. Concerning the La Palmerita granitoid (EOLP-05), the obtained weighted mean of 231.9 ± 2.3/3.5 (MSWD = 6.3, n = 24) Ma shows a very high MSWD, but is compatible with a similar emplacement age as the Marcabelí pluton.

The observed dispersion in the dates of ca. 20 Myr, in light of the high number of analyses performed, especially for the samples EOMP-01 and EOMP-10, could be interpreted as reflecting geological dispersion. Zircons from plutonic rocks are expected to record multiple events with the presence of antecrysts preserved from previous melting events from the source, or different melt injection events in the pluton itself (e.g. Samperton et al. 2015). In addition,

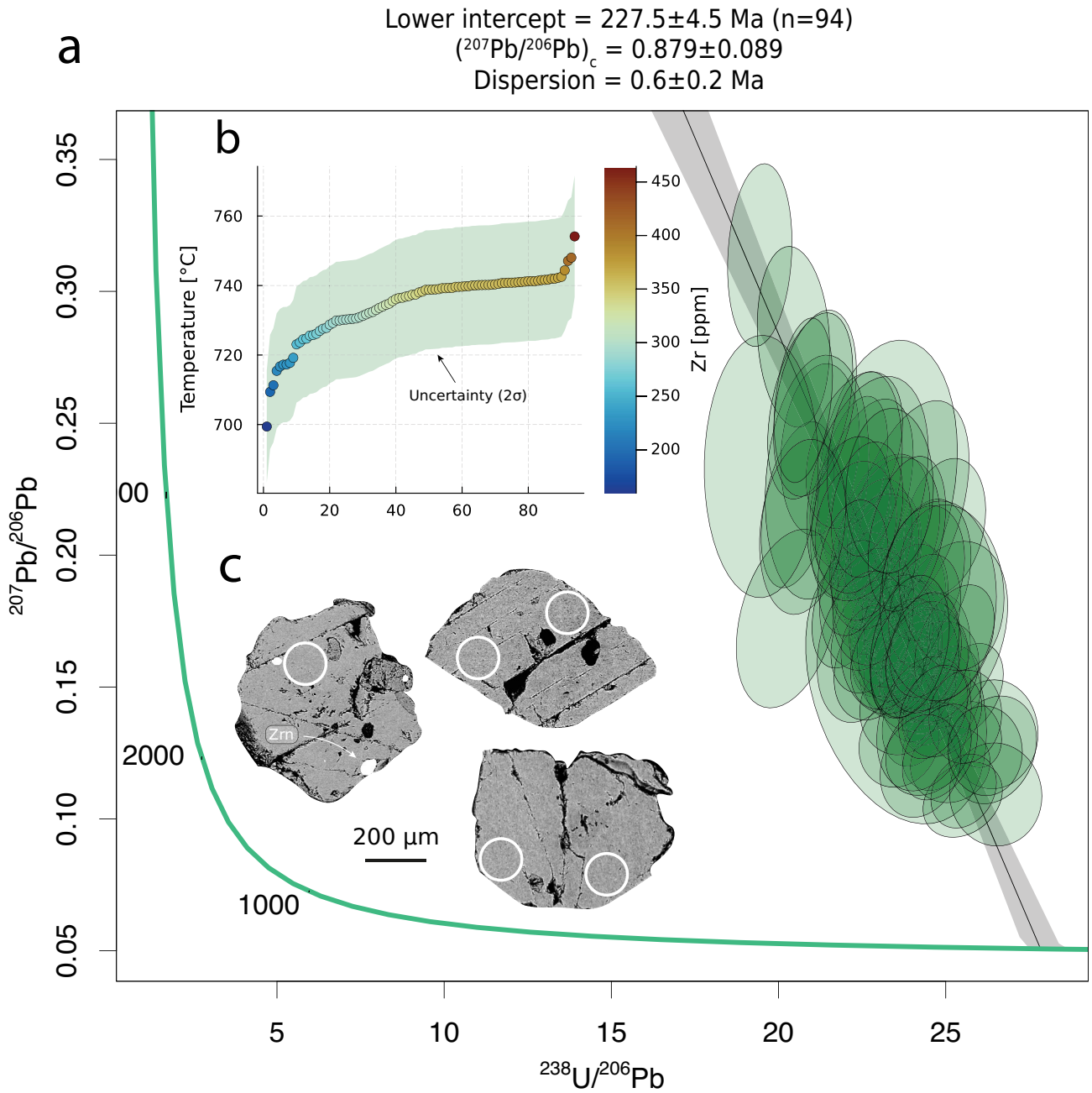


Fig. 12 **a** U–Pb titanite discordia age from the metagabbro sample EOPD-03 of the Piedras unit, calculated using IsoplotR (Vermeesch 2018). Ellipse uncertainties are reported at 2σ. The lower intercept yields an age of 227.5 ± 4.5 Ma with a dispersion of 0.6 ± 0.2 Ma. **b** Zr-in-titanite temperature estimates using the calibration from Hayden et al. (2008). **c** Representative backscattered images of the spot analyses (spot size = 64 µm) on the titanite grains. Zircon and rutile can be found as inclusions in the titanite

peraluminous melts are more prone to preserving such zircons due to their composition (Watson and Harrison 1983; Boehnke et al. 2013; Szymanowski et al. 2020). As such, some of the calculated weighted means have high MSWDs relative to the number of analyses, such as sample EOMP-10, with an MSWD of 6.5 for 68 analyses. These weighted means represent the peak of zircon crystallisation in each sample and are in good agreement with the corresponding KDE peaks (Fig. S5). However, given the uncertainty on the individual dates, they cannot be attributed to a distinct geological process during pluton assembly but rather serve as indicators of data dispersion with their associated MSWD. For instance, the monzogranite sample EOMP-10, which has the highest MSWD, shows that some of the individual dates used for the weighted mean calculation are not within uncertainty with each other, and that its rank-order plot

displays distinct plateaus (Fig. 4a, b), potentially recording discrete steps in the assembly of the pluton.

However, the current timescales commonly accepted for pluton emplacement, based mainly on TIMS data, are on the order of a few million years at most (Miller et al. 2007; De Saint Blanquat et al. 2011; Szymanowski et al. 2019). Furthermore, a long-term continuous magmatic emplacement over 20 Myr would likely produce a well-developed metamorphic contact aureole, which is not observed in the field. Thus, it may reflect distinct magmatic pulses separated by several million years and preserved at the sample scale, and/or reflect zircon crystallisation at the melting source or during extraction. These signals would then be masked by the high analytic uncertainty (2σ of 4–8 Myr per analysis on average). We therefore propose an emplacement age range for the Marcabelí pluton of 232–224 Ma, based on the two stages observed in sample EOMP-01 and the date distribution in sample EOMP-10, while acknowledging that the precision of this estimate is limited by the analytical uncertainties inherent to the method chosen in this study and is probably shorter. This could be further assessed in the future using a higher-precision method, such as TIMS, SIMS or a multicollector LA-ICP-MS.

Upper La Bocana migmatites: open system behaviour and an older magmatic event

The samples from Upper La Bocana show similar weighted means for analyses with Th/U ratios < 0.1, with ages ranging from 231.0 ± 2.4/3.6 (MSWD = 6.6, n = 20) to 223.9 ± 1.3/2.8 (MSWD = 3.3, n = 36) Ma. The large MSWD values indicate substantial scatter in the data, inconsistent with a single geological age. Instead, these data are consistent with a prolonged crustal melting event spanning ~ 15 Myr (ca. 220–235 Ma), potentially comprising a series of successive short-lived melt pulses. The two diatexite samples (EOLB-53 and EOLB-55) from Upper La Bocana yield older zircon dates that correlate with trace-element data and temperature estimates (Figs. 8a, 9 and 11a). This population shows dates ranging from ca. 240 to 260 Ma and a similar trace-element signature to the older La Palmerita analyses (Figs. 5b and 6b; dates spanning ca. 245 to 260 Ma). The dates recorded are younger than the depositional age estimated for the upper part of the sequence, El Tigre (maximum ca. 310 Ma), and are evidence of a post-depositional event, unless caused by concealed Pb-loss. The fact that both the La Palmerita granitoid and some migmatites from Upper La Bocana show the same signature of zircons suggests that part of the melt source of the La Palmerita granitoid is potentially derived from the Upper La Bocana diatexites.

The two samples from leucosomes of metatexite, EOLB-08 and particularly EOLB-10, also show a population with a high Th/U ratio, a distinct trace-element signature, and CL textures, but with dates similar to those of the other low Th/U analyses from these samples (Figs. 7b and 11b). These high Th/U analyses are from grains that record temperature estimates between 800 and 900 °C, higher than what the local rocks are estimated to have experienced at peak conditions, due to the absence of peritectic garnet in the area and *P–T* estimates from previous studies (Fig. S9 and Riel et al. 2013, 2016). The absence of garnet has been interpreted as evidence that the main melting reaction in Upper La Bocana is muscovite breakdown, which should occur around 680 °C at these pressure conditions (Riel et al. 2013). These low-temperature conditions are also unlikely to reset of the U–Pb isotopic system in zircon. Therefore, we interpret that zircons with similar dates but higher temperatures have been derived from a hotter source and show open-system behaviour, with melt from different sources emplaced at the scale of a leucosome. Concerning the low temperatures below the wet solidus, it is interpreted either as an underestimation of the activity of $aTiO_2$ in the melt, which would increase the temperature up to 70 °C or as a sign of disequilibrium crystallisation from melt or non-Henry's law substitution of Ti in zircon (e.g. Ferry and Watson 2007).

Lower La Bocana migmatites: multiple melting events

Zircon grains from Lower La Bocana (EOLB-04 and EOLB-37) locally show two distinct CL rims (Fig. 7c, grains 11 and 14), suggesting that some grains record multiple growth episodes. This is consistent with the dispersion observed in the calculated weighted means and the range of dates between ca. 215 and 235 Ma. Furthermore, the correlation observed between flat HREE and temperature estimates, especially for sample EOLB-04, suggests that zircons either record syn-growth with garnet (flat HREE, higher temperature), or cooling and melt crystallisation (steep HREE, lower temperature; Fig. 10). But the fact that no correlation between HREE and $^{206}Pb/^{238}U$ dates is observed is consistent with multiple growth episodes (Fig. S7). In metapelitic migmatites, most zircons are expected to grow during peak conditions, cooling, and crystallisation of the anatectic melt but not during the prograde metamorphic history (Roberts and Finger 1997; Schaltegger et al. 1999; Rubatto et al. 2006; Yakymchuk 2023). This is explained by the fact that the Zr content required in the melt to reach saturation increases with temperature, as predicted by zircon solubility models based on experiments (Watson and Harrison 1983; Kelsey et al. 2008; Boehnke et al. 2013; Crisp and Berry 2022). Due to the heterogeneous nature of a migmatite, and melt extraction and emplacement processes, cooling could happen locally before a reheating event, promoting the growth

of different generations of zircons recording similar Ti-temperatures and conditions. Zircons from the same sample could also preserve different histories due to the open-system nature of rocks with high melt fractions.

Titanite U–Pb ages and temperature estimates: constraints on reliability and gabbro cooling history

The closure temperature of Pb diffusion in titanite has been debated, with estimates ranging from 500 to 600 °C based on natural data and experimental work (e.g. Mezger et al. 1991; Cherniak 1993; Spear and Parrish 1996; Tucker et al. 2004). In a recent review, Kohn (2017) argued that the closure temperature should be much higher, and that chronological resetting should be ineffective below 800 °C, and we follow this interpretation here. Given that the natural intracrystalline gradient for Zr is at least as steep as that for Pb (Stearns et al. 2016), Zr diffusion should be equally limited below 800 °C. The large grain size in this study (300–500 µm) and the Zr-in-titanite temperature estimates (~700 to 760 °C) therefore support the U–Pb age and temperature estimates as records of titanite crystallisation rather than diffusive resetting. These temperatures may additionally be overestimated by 40–80 °C, as the Hayden et al. (2008) thermometer was calibrated for {111} sector chemistry, whereas analyses here were performed on unoriented grains, further placing titanite below the closure temperatures of both Zr and Pb.

The homogeneous temperature estimates and well-defined discordia age of 227.5 ± 4.5 Ma with a similar temperature range across most analyses support the idea of a single generation of titanite, which we interpret as metamorphic based on petrographic evidence (see Fig. S1). Although a magmatic origin cannot be entirely ruled out, the sub-euhedral morphology, absence of oscillatory zoning in BSE imaging, lack of reaction rims, and the predominantly metamorphic character of the host rock are more consistent with metamorphic growth. We interpret this age as a record of hydration and metamorphism that formed the amphibole, which is associated with the cooling of the gabbro's magmatic stage. This is within the uncertainty of the two zircon crystallisation ages, interpreted as magmatic, and the amphibole cooling age, interpreted as metamorphic, previously reported in the same unit (Noble et al. 1997; Gabriele 2002; Cochrane et al. 2014). This suggests that the magmatism and the metamorphism linked to the cooling of the gabbro occur in rapid succession. A more precise magmatic age would be helpful in the future, as Noble et al. (1997) report an age with only two analyses, and Cochrane et al. (2014) report very low U content in their analyses, producing high uncertainties.

Relationship between migmatites and granitoids

To better characterise the differences and similarities between the zircon analyses from the granitoids and the migmatites, a discrimination diagram that uses $\log_{10}$ ratios of Ce/U and Th/U from Roberts et al. (2024) is used (Fig. 13). Three granitoid groups are represented by 2D KDE envelopes (50% and 95%) derived from compiled data of Himalayan granitoids by Roberts et al. (2024). These three groups are interpreted respectively as S-type, hybrid, and I-type. Zircon analyses from the two granitoids, Marcabelí and La Palmerita, are plotted alongside analyses from the migmatites on top of these groups. The four samples of the Marcabelí pluton cluster in the domain of hybrid S-types, with $\log_{10}$(Th/U) values between −0.9 and 0.2 and $\log_{10}$(Ce/U) values between −2.8 and 2.5. A significant number of analyses, especially from the sample EOMP-01, also show $\log_{10}$(Th/U) values below −1, with considerable spread. Sample EOLP-05 from the La Palmerita granitoid exhibits a notable clustering in the pure S-type field, with values ranging from −2 to −1.5 for $\log_{10}$(Th/U) and from −3.8 to −3 for $\log_{10}$(Ce/U). The trace element chemistry of the zircons suggests a slightly different source between the Marcabelí pluton and the La Palmerita granitoid. The Marcabelí pluton shows a mixed signature between I-type and S-type signatures, whereas most of the analyses from the La Palmerita granitoid have a pure S-type composition (Fig. 7). This is supported by the presence of hornblende in the field and mafic enclaves (Fig. 2a-b) for the Marcabelí pluton, and the presence of centimetre-scale patches of sillimanite and muscovite for the La Palmerita granitoid. Finally, the five older analyses from the La Palmerita sample cluster in the same field as some analyses from the migmatites of the Upper La Bocana samples (EOLB-53 and EOLB-55) within the overlapping field between hybrid S-type and I-type granitoids, and show similar dates and characteristics as previously discussed. The Lower La Bocana migmatites exhibit the highest degree of partial melting in the observed sequence, as evidenced by the presence of peritectic garnet. At least two zircon growth generations resolved in these samples, sometimes separated by a few Myr, support multiple episodes of melting and crystallisation, or at least of zircon growth (e.g. Fig. 7c grain 14).

Another observation is the absence of zircons showing flat HREE patterns in the granitoid samples that could have been recorded by antecrysts formed in the melt source before emplacement, if the melt was produced during Bt-breakdown and with peritectic garnet (Fig. 6), especially in regard to the large number of zircon analysed in this study. It may indicate that migmatitic zircons predominantly record post-melting cooling, whereas the melt extracted from them and emplaced in plutons in the middle to upper crust would

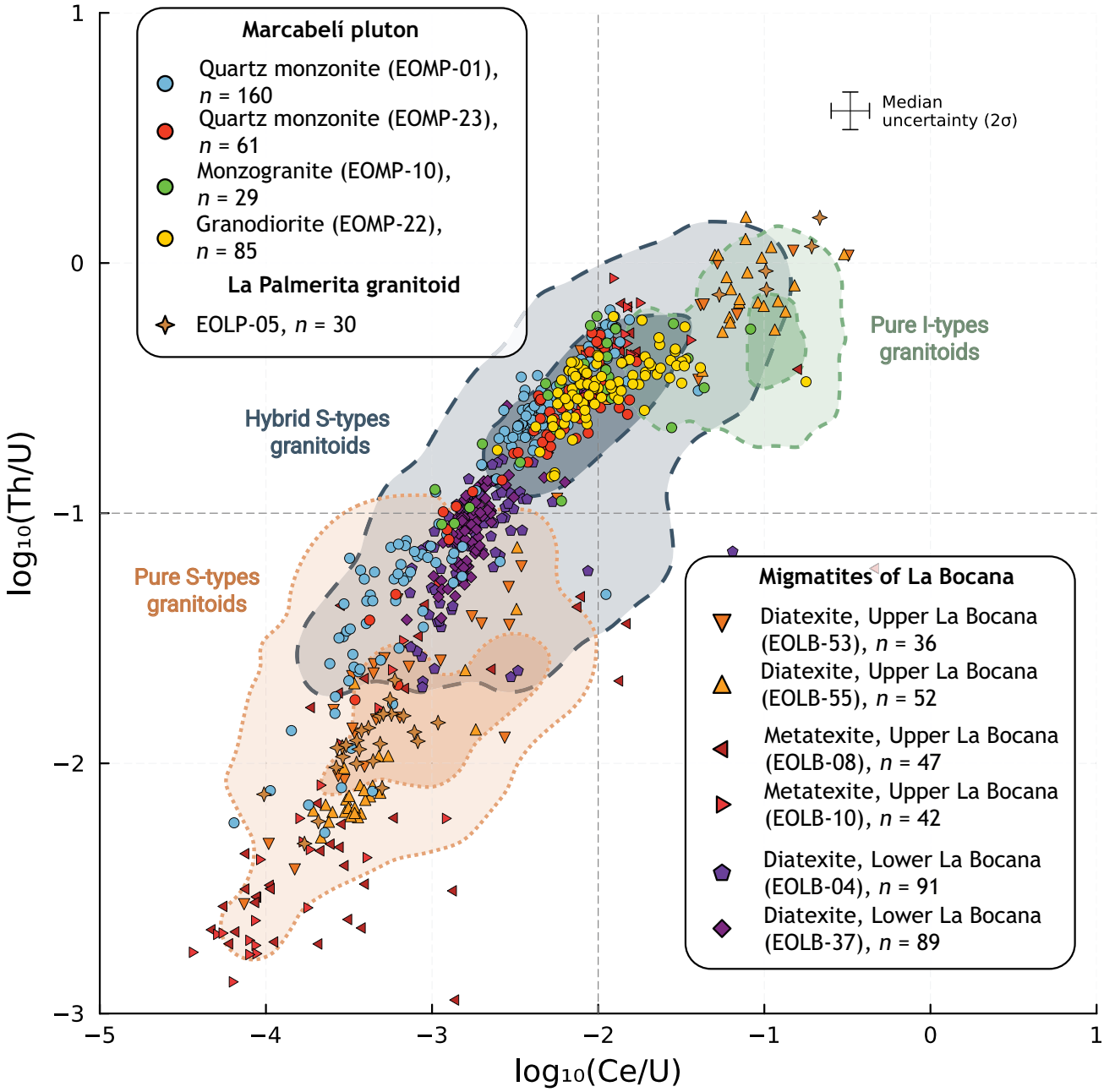


Fig. 13 Discrimination diagram using $\log_{10}$(Ce/U) vs. $\log_{10}$(Th/U) from zircon trace elements. All the zircon analyses from the igneous samples with Ce measured and all analyses from the migmatites are reported from concordant dates younger than 270 Ma. The three groups of dark and lighter contours represent 2D KDE envelopes including 50 and 95% from the compiled data of different granitoids from Roberts et al. (2024)

crystallise faster. Therefore, the granitoids in the middle to upper crust would be formed predominantly from melt produced during prograde metamorphism, with melting dominated by Ms-breakdown in the metapelites of the Lower La Bocana unit. The cooling of the lower-crustal migmatites would occur later than the upper-crustal plutons, due to their depth, meaning that zircons would crystallise from the trapped melts or during retrogression later in time. A more precise analytical method, such as TIMS or SIMS, may help to decipher if the granitoids are generally younger than the zircons showing syn-growth with garnet in the Lower La Bocana unit to confirm this interpretation (Fig. 14).

Tectonic implications for the El Oro complex

Integration of geochronological data from all samples in this study enables a more robust reconstruction of the Triassic event in the EOC. The main results of this study are

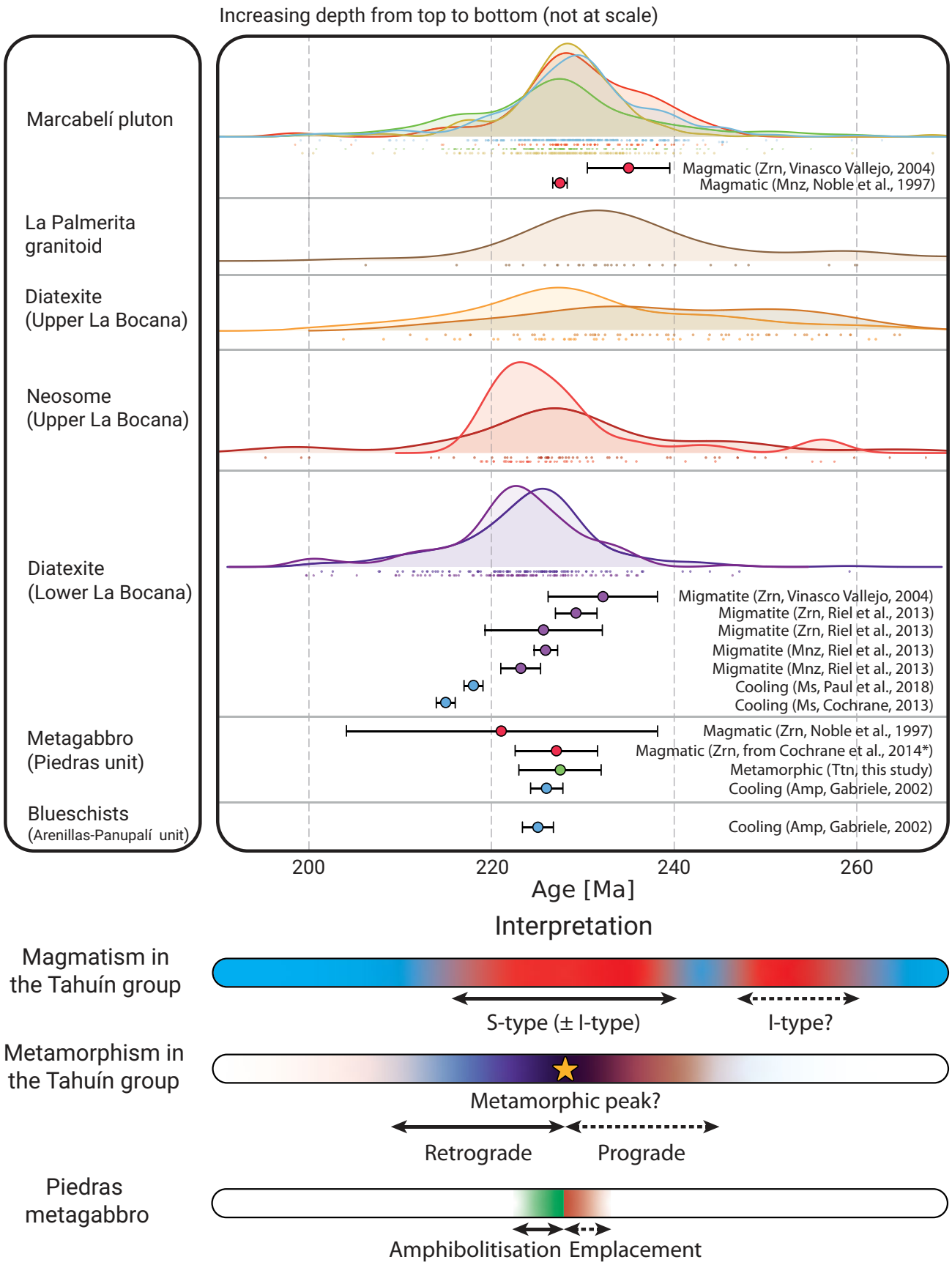

Increasing depth from top to bottom (not at scale)
Marcabelí pluton
La Palmerita granitoid
Diatexite (Upper La Bocana)
Neosome (Upper La Bocana)
Diatexite (Lower La Bocana)
Metagabbro (Piedras unit)
Blueschists (Arenillas-Panupalí unit)
Magmatic (Zrn, Vinasco Vallejo, 2004)
Magmatic (Mnz, Noble et al., 1997)
Migmatite (Zrn, Vinasco Vallejo, 2004)
Migmatite (Zrn, Riel et al., 2013)
Migmatite (Zrn, Riel et al., 2013)
Migmatite (Mnz, Riel et al., 2013)
Migmatite (Mnz, Riel et al., 2013)
Cooling (Ms, Paul et al., 2018)
Cooling (Ms, Cochrane, 2013)
Magmatic (Zrn, Noble et al., 1997)
Magmatic (Zrn, from Cochrane et al., 2014*)
Metamorphic (Ttn, this study)
Cooling (Amp, Gabriele, 2002)
Cooling (Amp, Gabriele, 2002)
200
220
240
260
Age [Ma]
Interpretation
Magmatism in the Tahuín group
S-type (± I-type)
I-type?
Metamorphism in the Tahuín group
Metamorphic peak?
Retrograde
Prograde
Piedras metagabbro
Amphibolitisation
Emplacement

Fig. 14 Summary figure of the geochronological data from the El Oro complex collected in this study and from the literature. Each kernel density estimate corresponds to the analysis of one sample. The magmatic age of Cochrane et al. (2014) was recalculated by removing 4 analyses with dates below 220 Ma that were interpreted as metamorphic and therefore outliers. An interpretation of the timing of the major events in the El Oro complex for the Triassic event is also provided

reported in Fig. 14 with an interpretation of the main geological events on the scale of the EOC. A new melting event between ca. 245 and 260 Ma is reported and is interpreted to have produced magmatism with an I-type-like signature based on age and zircon trace element data from the Upper La Bocana (EOLB-53 and 55) and the La Palmerita granitoid (EOLP-05). The main magmatic event of the Tahuín group is shown to take place between ca. 220 to 230 Ma, associated with the emplacement of the major S-type plutons in the EOC. The duration of the prograde history is poorly constrained, but the metamorphic peak is interpreted to occur at ca. 228 Ma. This timing corresponds to the end of the emplacement of the Piedras gabbros and the beginning of the cooling of the sequence by the underplating of the blueschists of the Arenillas-Panupalí unit (Gabriele 2002; Riel et al. 2014). This is supported by the new high-temperature (~740 ± 20 °C) titanite metamorphic age obtained in this study, which we interpret as recording the onset of cooling of the sequence. The zircon dates in the migmatites might record the regional prograde and retrograde history during ca. 20 Myr, between approximately 235 and 220 Ma. In this case, the zircons in Lower La Bocana would reflect multiple heat pulses at the sample scale, as indicated by multiple syn- and post-garnet zircon populations, whose HREE slopes show no correlation with age (Figs. 10, S7). Previous ages reported for the plutons and the migmatites from the La Bocana unit all fall within these ranges (Noble et al. 1997; Vinasco Vallejo 2004; Riel et al. 2013). Cooling ages in the Lower La Bocana unit, determined by $^{40}Ar/^{39}Ar$ in muscovite from 218 to 214 Ma, then show the subsequent cooling of the sequence (Cochrane 2013; Paul et al. 2018).

These data are mostly compatible with the geodynamic interpretation of the Triassic event in the EOC proposed by Riel et al. (2014) with the addition of the first identification of zircon domains that record dates between ca. 245 and 260 Ma in the Upper La Bocana (EOLB-55 and EOLB-53, Fig. 11). We propose that it is the result of the injection of a mantle-derived melt into the lower parts of the Tahuín Group, which may correspond to a crystalline basement that is not preserved in the current record. This triggered partial melting of the crust, supported by the I-type-like signature in the zircons, which could form in a crustal contaminated setting (Fig. 13). This suggests some form of crustal thinning as early as ca. 260 Ma in the EOC. This thinning allowed mantle decompression and melting in this scenario. The subsequent history is similar to the one proposed by Riel et al. (2014): the underplating of the Arenillas-Panupalí blueschists below the Piedras unit occurred at ca. 226 Ma, as supported by $^{40}Ar/^{39}Ar$ ages on hornblende on both the Arenillas-Panupalí and the Piedras units (Gabriele 2002), which allowed the quenching of the metamorphic sequence and the end of the heat source.

Constraining more precisely the timescale between melt production, transport through the crust, and injection into the pluton is hindered by two reasons: (i) the analytical and spatial precision of targeting zircon rims is generally too low, and (ii) the difficulty in relating zircon ages within leucosomes to zircon ages within the pluton. These problems arise because plutons were likely formed by many short-term melt injections, that overlap within analytical uncertainty. However, it is clear that the zircons from the source metasedimentary rocks can preserve evidence of multiple crystallisation events, particularly in trace elements at the sample scale. In the future, high analytical and spatial precision analysis or the combination with other minerals, such as monazite, may be able to constrain these pulses more precisely. Furthermore, additional zircon isotopic systematics, such as $^{176}Hf/^{177}Hf$ or $\delta^{18}O$, could be used to further assess the relative contributions of metasediment-derived melt and the mafic component from the Piedras metagabbro to the Marcabelí pluton and to the migmatites showing evidence of open-system behaviour, as zircons are expected to preserve the isotopic signatures of these distinct source reservoirs (e.g. Griffin et al. 2002; Valley 2003; Yang et al. 2006; Wei et al. 2008; Gagnevin et al. 2011).

Conclusions

This study presents a detailed analysis of zircon U–Pb and trace element data, highlighting the complexities involved in interpreting the ages between S-type and hybrid (S-type and I-type) granitoids and migmatitic systems. The findings emphasise the challenges posed by geological factors such as inheritance, and the long-lived nature of melting and (re) crystallisation processes.

The analysis of the Marcabelí pluton confirms that the main emplacement occurred during prograde metamorphism. It is proposed that multiple pulses, separated by few Myr, are responsible for the pluton assembly, as suggested by the high dispersion in the dates in each sample. Concerning the La Palmerita granitoid, trace element data and CL images of the older grains suggest that this granitoid shares a genetic link with the migmatites from Upper La Bocana. In the Upper La Bocana unit, trace-element data and textural evidence indicate that some migmatitic samples exhibit open-system behaviour, while others record an older magmatic event, between ca. 260 and 245 Ma. Many of the

zircons in the Lower La Bocana unit form in equilibrium with garnet, consistent with the presence of peritectic garnets. Overall, the zircon dates indicate that zircon crystallisation in the La Bocana unit occurred between 235 and 215 Ma. The study also highlights the rapid cooling of the gabbro emplacement from the Piedras unit, supported by a titanite age of 227.5 ± 4.5 (n = 94) Ma and temperature estimates around 740 °C.

These findings confirm that the main source of melt for the Marcabelí pluton and La Palmerita granitoid is the migmatites of the La Bocana unit. The timescale for assembling a sediment-derived pluton is therefore inherently constrained by the rate of melt production in the metasedimentary source. This rate is, in turn, controlled by the pace of tectonically driven increases in temperature and pressure, or, more generally, by heating rates, that may result from a combination of thermal diffusion and tectonic processes such as crustal thinning. Therefore, the geochronological data in this study suggest that the timescales of pluton assembly may be on the order of a few to tens of millions of years in these settings, contrary to previous studies of dominantly I-type pluton assembly (ca. 100 years to a few Myr, e.g. De Saint Blanquat et al. 2011).

Overall, this work highlights the appeal of combining U–Pb and trace-element data to analyse a large number of magmatic and metamorphic zircons per sample and quantify the complexity of melt processes. This approach provides valuable insights into the temporal and thermal evolution of these magmatic and metamorphic systems, emphasising the importance of prolonged and episodic processes in the development of complex plutonic bodies such as the Marcabelí pluton and in migmatites. However, coupling with other minerals and systematics, as well as with other analytical methods, could help more precisely decipher the complexity observed at the sample scale. Finally, this study shows that studying systems in which both the potential source and the final product of melting processes are accessible is a valuable approach for constraining these processes.

Supplementary Information The online version contains supplementary material available at https://doi.org/10.1007/s00410-026-02346-5.

Acknowledgements The authors thank C. Ganade for his assistance in the field and thought-provoking discussions. Hugo Dominguez thanks D. Rubatto and J-F. Moyen for discussions concerning zircon geochronology, L. Pacchiega and A. Berger for assistance in operating Bern's different SEMs and in the process of mineral separation, and M. Lueder for discussions concerning closure temperature estimates. Hugo Dominguez acknowledges funding from the Institute of Multiscale Modelling (M3ODEL) in Mainz and the German Federal Ministry of Economic Affairs and Climate Action (BMWK) (grant number 03EE4071B). Mahyra Tedeschi acknowledges the National Council for Scientific and Technological Development (CNPq) for her scientific research productivity grant (308733/2021-5). Nicolas Riel acknowledges the German Research Foundation (DFG) – project number #521637679. The authors thank three anonymous reviewers for their comments which improved this work, and editor Hans Keppler for the careful handling of the manuscript.

Author contributions H. Dominguez, R. Tamblyn, and P. Lanari contributed to the study conception and design. P. Lanari acquired the funding. Field work and sample collection were carried out by H. Dominguez, P. Lanari, M. Tedeshi, N. Riel, J. Forshaw, E. Jaillard, and S. Macías-Mosquera. Sample preparation was performed by H. Dominguez and J. Forshaw, and data acquisition and reduction were conducted by H. Dominguez and R. Tamblyn. Data treatment was done by H. Dominguez. The first draft of the manuscript was written by H. Dominguez, and all authors commented on previous versions. All authors read and approved the final manuscript.

Funding Open Access funding enabled and organized by Projekt DEAL. Funding for this study was provided by the European Research Council (ERC) under the European Union's Horizon 2020 research and innovation programme (grant agreement No 850530). Open access funding was provided by the Johannes Gutenberg University.

Data availability The complete, unfiltered datasets of zircon and titanite analyses produced in this study, along with the GPS locations of all the samples used, are available in the supplementary material.

Open Access This article is licensed under a Creative Commons Attribution 4.0 International License, which permits use, sharing, adaptation, distribution and reproduction in any medium or format, as long as you give appropriate credit to the original author(s) and the source, provide a link to the Creative Commons licence, and indicate if changes were made. The images or other third party material in this article are included in the article's Creative Commons licence, unless indicated otherwise in a credit line to the material. If material is not included in the article's Creative Commons licence and your intended use is not permitted by statutory regulation or exceeds the permitted use, you will need to obtain permission directly from the copyright holder. To view a copy of this licence, visit http://creativecommons.org/licenses/by/4.0/.

References

Aleinikoff JN, Wintsch RP, Tollo RP, Unruh DM, Fanning CM, Schmitz MD (2007) Ages and origins of rocks of the Killingworth dome, south-central Connecticut: Implications for the tectonic evolution of southern New England. Am J Sci 307:63–118. https://doi.org/10.2475/01.2007.04

Andersen T, Elburg MA, Magwaza BN (2019) Sources of bias in detrital zircon geochronology: Discordance, concealed lead loss and common lead correction. Earth-Sci Rev 197:102899. https://doi.org/10.1016/j.earscirev.2019.102899

Annen C (2011) Implications of incremental emplacement of magma bodies for magma differentiation, thermal aureole dimensions and plutonism–volcanism relationships. Tectonophysics 500:3–10. https://doi.org/10.1016/j.tecto.2009.04.010

Asimus JL, Daczko NR, Gazi J, Ezad IS, Belousov I, Rodemann T, Halpin JA, Piazolo S (2024) Experimental Replacement of Zircon by Melt-Mediated Coupled Dissolution-Precipitation Causes Dispersion in U–Pb Ages. J Metamorph Geol 42:1179–1195. https://doi.org/10.1111/jmg.12795

Aspden JA, Bonilla W, Duque P (1995) The El Oro metamorphic complex, Ecuador: geology and economic mineral deposits. British Geological Survey, Keyworth, Nottingham

Baldock JW (1982) Geology of Ecuador: explanatory bulletin of the national geological map of the Republic of Ecuador; 1: 1,000,000 scale 1982. Ministerio de Recursos Naturales y Energéticos, Dirección General de Geología y Minas

Ballard JR, Palin JM, Campbell IH (2002) Relative oxidation states of magmas inferred from Ce(IV)/Ce(III) in zircon: application to porphyry copper deposits of northern Chile. Contrib Mineral Petrol 144:347–364. https://doi.org/10.1007/s00410-002-0402-5

Bezanson J, Edelman A, Karpinski S, Shah VB (2017) Julia: A Fresh Approach to Numerical Computing. SIAM Rev 59:65–98. https://doi.org/10.1137/141000671

Bloch EM, Jollands MC, Tollan P, Plane F, Bouvier A-S, Hervig R, Berry AJ, Zaubitzer C, Escrig S, Müntener O, Ibañez-Mejia M, Alleon J, Meibom A, Baumgartner LP, Marin-Carbonne J, Newville M (2022) Diffusion anisotropy of Ti in zircon and implications for Ti-in-zircon thermometry. Earth Planet Sci Lett 578:117317. https://doi.org/10.1016/j.epsl.2021.117317

Boehnke P, Watson EB, Trail D, Harrison TM, Schmitt AK (2013) Zircon saturation re-revisited. Chem Geol 351:324–334. https://doi.org/10.1016/j.chemgeo.2013.05.028

Brown M (2013) Granite: From genesis to emplacement. Geol Soc Am Bull 125:1079–1113. https://doi.org/10.1130/B30877.1

Cashman KV, Sparks RSJ, Blundy JD (2017) Vertically extensive and unstable magmatic systems: A unified view of igneous processes. Science 355:eaag3055. https://doi.org/10.1126/science.aag3055

Cherniak DJ (1993) Lead diffusion in titanite and preliminary results on the effects of radiation damage on Pb transport. Chem Geol 110:177–194. https://doi.org/10.1016/0009-2541(93)90253-F

Cherniak DJ (2010) Diffusion in Accessory Minerals: Zircon, Titanite, Apatite, Monazite and Xenotime. Rev Mineral Geochem 72:827–869. https://doi.org/10.2138/rmg.2010.72.18

Cherniak DJ, Watson EB (2001) Pb diffusion in zircon. Chem Geol 172:5–24. https://doi.org/10.1016/S0009-2541(00)00233-3

Cherniak DJ, Hanchar JM, Watson EB (1997) Rare-earth diffusion in zircon. Chem Geol 134:289–301. https://doi.org/10.1016/S0009-2541(96)00098-8

Cochrane R (2013) U-Pb thermochronology, geochronology and geochemistry of NW South America: rift to drift transition, active margin dynamics and implications for the volume balance of continents. Université de Genève

Cochrane R, Spikings R, Gerdes A, Ulianov A, Mora A, Villagómez D, Putlitz B, Chiaradia M (2014) Permo-Triassic anatexis, continental rifting and the disassembly of western Pangaea. Lithos 190–191:383–402. https://doi.org/10.1016/j.lithos.2013.12.020

Cózar P, Díaz-Martínez E, Carlotto V (2024) Foraminiferal biostratigraphy of the pennsylvanian cerro prieto formation, amotape mountains, NW Peru: Correlation with the Central Andean basin. J South Am Earth Sci 146:105086. https://doi.org/10.1016/j.jsames.2024.105086

Crisp LJ, Berry AJ (2022) A new model for zircon saturation in silicate melts. Contrib Mineral Petrol 177:71. https://doi.org/10.1007/s00410-022-01925-6

Daczko NR, Elliott V, Piazolo S, Hao K (2024) Zircon Coupled Dissolution–Precipitation Replacement During Melt–Rock Interaction Modifies Chemical Signatures Resulting in Misleading Ages. J Metamorph Geol 42:1197–1214. https://doi.org/10.1111/jmg.12796

De Saint Blanquat M, Horsman E, Habert G, Morgan S, Vanderhaeghe O, Law R, Tikoff B (2011) Multiscale magmatic cyclicity, duration of pluton construction, and the paradoxical relationship between tectonism and plutonism in continental arcs. Tectonophysics 500:20–33. https://doi.org/10.1016/j.tecto.2009.12.009

Farina F, Stevens G, Gerdes A, Frei D (2014) Small-scale Hf isotopic variability in the Peninsula pluton (South Africa): the processes that control inheritance of source 176Hf/177Hf diversity in S-type granites. Contrib Mineral Petrol 168:1065. https://doi.org/10.1007/s00410-014-1065-8

Farina F, Dini A, Davies JHFL, Ovtcharova M, Greber ND, Bouvier A-S, Baumgartner L, Ulianov A, Schaltegger U (2018) Zircon petrochronology reveals the timescale and mechanism of anatectic magma formation. Earth Planet Sci Lett 495:213–223. https://doi.org/10.1016/j.epsl.2018.05.021

Feininger T (1978) Geologic map of western El Oro province. Esc Politec Nac Quito Ecuad

Feininger T (1982) The metamorphic basement of Ecuador. Geol Soc Am Bull 93:87 https://doi.org/10.1130/0016-7606(1982)93%26lt;87:TMBOE%26gt;2.0.CO;2

Ferry JM, Watson EB (2007) New thermodynamic models and revised calibrations for the Ti-in-zircon and Zr-in-rutile thermometers. Contrib Mineral Petrol 154:429–437. https://doi.org/10.1007/s00410-007-0201-0

Gabriele P (2002) HP terranes exhumation in active margin setting: Geology, petrology and geochemistry of the Raspas Complex in SW Ecuador. Phdthesis. Université de Lausanne (Suisse)

Gagnevin D, Daly JS, Horstwood MSA, Whitehouse MJ (2011) In-situ zircon U–Pb, oxygen and hafnium isotopic evidence for magma mixing and mantle metasomatism in the Tuscan Magmatic Province, Italy. Earth Planet Sci Lett 305:45–56. https://doi.org/10.1016/j.epsl.2011.02.039

Gordon SM, Whitney DL, Teyssier C, Grove M, Dunlap WJ (2008) Timescales of migmatization, melt crystallization, and cooling in a Cordilleran gneiss dome: Valhalla complex, southeastern British Columbia. Tectonics 27:2007TC002103. https://doi.org/10.1029/2007TC002103

Gordon SM, Bowring SA, Whitney DL, Miller RB, McLean N (2010) Time Scales of Metamorphism, Deformation, and Crustal Melting in a Continental Arc, North Cascades USA. Geol Soc Am Bull 122:1308–1330. https://doi.org/10.1130/B30060.1

Griffin W, Wang X, Jackson S, Pearson N, O'Reilly SY, Xu X, Zhou X (2002) Zircon chemistry and magma mixing, SE China: in-situ analysis of Hf isotopes, Tonglu and Pingtan igneous complexes. Lithos 61:237–269 https://doi.org/10.1016/S0024-4937(02)00082-8

Gulson BL, Krogh TE (1973) Old lead components in the young Bergell Massif, south-east Swiss Alps. Contrib Mineral Petrol 40:239–252. https://doi.org/10.1007/BF00373788

Harris NBW, Caddick M, Kosler J, Goswami S, Vance D, Tindle AG (2004) The pressure–temperature–time path of migmatites from the Sikkim Himalaya. J Metamorph Geol 22:249–264. https://doi.org/10.1111/j.1525-1314.2004.00511.x

Hawkesworth C, Dhuime B, Pietranik A, Cawood P, Kemp A, Storey C (2010) The generation and evolution of the continental crust. J Geol Soc 167:229–248. https://doi.org/10.1144/0016-76492009-072

Hayden LA, Watson EB, Wark DA (2008) A thermobarometer for sphene (titanite). Contrib Mineral Petrol 155:529–540. https://doi.org/10.1007/s00410-007-0256-y

Hinton RW, Upton BGJ (1991) The chemistry of zircon: Variations within and between large crystals from syenite and alkali basalt xenoliths. Geochim Cosmochim Acta 55:3287–3302. https://doi.org/10.1016/0016-7037(91)90489-R

Horstwood MSA, Košler J, Gehrels G, Jackson SE, McLean NM, Paton C, Pearson NJ, Sircombe K, Sylvester P, Vermeesch P, Bowring JF, Condon DJ, Schoene B (2016) Community-Derived Standards for U-(Th-)Pb Geochronology – Uncertainty Propagation, Age Interpretation and Data Reporting. Geostand Geoanalytical Res 40:311–332. https://doi.org/10.1111/j.1751-908X.2016.00379.x

Huber PJ, Ronchetti EM (2009) Robust Statistics, 1st edn. Wiley https://doi.org/10.1002/9780470434697

Iddings A, Olsson AA (1928) Geology of Northwest Peru. AAPG Bull 12:1–39. https://doi.org/10.1306/3D9327D7-16B1-11D7-8645000102C1865D

Jackson SE, Pearson NJ, Griffin WL, Belousova EA (2004) The application of laser ablation-inductively coupled plasma-mass spectrometry to in situ U–Pb zircon geochronology. Chem Geol 211:47–69. https://doi.org/10.1016/j.chemgeo.2004.06.017

Jaupart C, Mareschal J-C (eds) (2010) Global energy budget Crust, mantle and core. Heat Gener Transp Earth https://doi.org/10.1017/CBO9780511781773.009

Jochum KP, Willbold M, Raczek I, Stoll B, Herwig K (2005) Chemical Characterisation of the USGS Reference Glasses GSA-1G, GSC-1G, GSD-1G, GSE-1G, BCR-2G, BHVO-2G and BIR-1G Using EPMA, ID-TIMS, ID-ICP-MS and LA-ICP-MS. Geostand Geoanalytical Res 29:285–302. https://doi.org/10.1111/j.1751-908X.2005.tb00901.x

Jochum KP, Weis U, Stoll B, Kuzmin D, Yang Q, Raczek I, Jacob DE, Stracke A, Birbaum K, Frick DA, Günther D, Enzweiler J (2011) Determination of Reference Values for NIST SRM 610–617 Glasses Following ISO Guidelines. Geostand Geoanalytical Res 35:397–429. https://doi.org/10.1111/j.1751-908X.2011.00120.x

Keller CB (2023) Isoplot.jl. https://doi.org/10.17605/OSF.IO/Z37WE

Kelsey DE, Clark C, Hand M (2008) Thermobarometric modelling of zircon and monazite growth in melt-bearing systems: examples using model metapelitic and metapsammitic granulites. J Metamorph Geol 26:199–212. https://doi.org/10.1111/j.1525-1314.2007.00757.x

Kemp AIS, Hawkesworth CJ, Foster GL, Paterson BA, Woodhead JD, Hergt JM, Gray CM, Whitehouse MJ (2007) Magmatic and Crustal Differentiation History of Granitic Rocks from Hf-O Isotopes in Zircon. Science 315:980–983. https://doi.org/10.1126/science.1136154

Kohn MJ (2017) Titanite Petrochronology. Rev Mineral Geochem 83:419–441. https://doi.org/10.2138/rmg.2017.83.13

Korenaga J (2018) Crustal evolution and mantle dynamics through Earth history. Philos Trans R Soc Math Phys Eng Sci 376:20170408. https://doi.org/10.1098/rsta.2017.0408

Kunz BE, Manzotti P, Von Niederhäusern B, Engi M, Darling JR, Giuntoli F, Lanari P (2018) Permian high-temperature metamorphism in the Western Alps (NW Italy). Int J Earth Sci 107:203–229. https://doi.org/10.1007/s00531-017-1485-6

Kylander-Clark ARC, Hacker BR, Cottle JM (2013) Laser-ablation split-stream ICP petrochronology. Chem Geol 345:99–112. https://doi.org/10.1016/j.chemgeo.2013.02.019

Li Y, Xie H, Dong C, Wang S, Wan Y (2022) Zircon evolution from migmatite to crustally-derived granite: A case study of late Neoarchean migmatite in the Yishan area, western Shandong, North China Craton. Gondwana Res 112:82–104. https://doi.org/10.1016/j.gr.2022.09.008

Litherland M (1994) The metamorphic belts of Ecuador. Overseas Mem Br Geol Surv 11:1–147

Martínez M (1970) Geología del basamento Paleozóico en las Montañas de Amotape y posible origen del petróleo en las rocas Paleozóicas del noreste de Perú. Primer Congr Latinoam Geol 2:105–138

McDonough WF, Sun S (1995) The composition of the Earth. Chem Geol 120:223–253. https://doi.org/10.1016/0009-2541(94)00140-4

Mezger K, Rawnsley CM, Bohlen SR, Hanson GN (1991) U-Pb Garnet, Sphene, Monazite, and Rutile Ages: Implications for the Duration of High-Grade Metamorphism and Cooling Histories, Adirondack Mts., New York. J Geol 99:415–428. https://doi.org/10.1086/629503

Michel J, Baumgartner L, Putlitz B, Schaltegger U, Ovtcharova M (2008) Incremental growth of the Patagonian Torres del Paine laccolith over 90 k.y. Geology 36:459. https://doi.org/10.1130/G24546A.1

Miller JS, Matzel JEP, Miller CF, Burgess SD, Miller RB (2007) Zircon growth and recycling during the assembly of large, composite arc plutons. J Volcanol Geotherm Res 167:282–299. https://doi.org/10.1016/j.jvolgeores.2007.04.019

Mourier T (1988) La transition entre Andes marginales et Andes cordilléraines à ophiolites: évolution sédimentaire, magmatique et structurale du relais de Huancabamba (3 a 8 Lat. S ; Nord Pérou-Sud Équateur). These de doctorat. Paris 11

Murali AV, Parthasarathy R, Mahadevan TM, Das MS (1983) Trace element characteristics, REE patterns and partition coefficients of zircons from different geological environments—A case study on Indian zircons. Geochim Cosmochim Acta 47:2047–2052. https://doi.org/10.1016/0016-7037(83)90220-X

Nasdala L, Wenzel M, Vavra G, Irmer G, Wenzel T, Kober B (2001) Metamictisation of natural zircon: accumulation versus thermal annealing of radioactivity-induced damage. Contrib Mineral Petrol 141:125–144. https://doi.org/10.1007/s004100000235

Nasdala L, Zhang M, Kempe U, Panczer G, Gaft M, Andrut M, Plötze M (2003) Spectroscopic methods applied to zircon. Rev Mineral Geochem 53:427–467 https://doi.org/10.2113/0530427

Noble SR, Aspden JA, Jemielita R (1997) Northern Andean crustal evolution: New U-Pb geochronological constraints from Ecuador. Geol Soc Am Bull 109:789–798. https://doi.org/https:// https://doi.org/10.1130/0016-7606(1997)109%3C0789:NACENU%3E2.3.CO;2

Norris A, Danyushevsky L (2018) Towards estimating the complete uncertainty budget of quantified results measured by LA-ICP-MS. Goldschmidt Boston MA USA

Oldman CJ, Warren CJ, Harris NBW, Kunz BE, Spencer CJ, Argles TW, Roberts NMW, Hammond SJ, Degli-Alessandrini G (2025) Melt reactions and timescales of melting in pelitic rocks—a case study from the Garhwal Himalaya. Contrib Mineral Petrol 180:62. https://doi.org/10.1007/s00410-025-02247-z

Oliver GJH, Corfu F, Krogh TE (1993) U-Pb ages from SW Poland: evidence for a Caledonian suture zone between Baltica and Gondwana. J Geol Soc 150:355–369. https://doi.org/10.1144/gsjgs.150.2.0355

Paterson BA, Stephens WE, Rogers G, Williams IS, Hinton RW, Herd DA (1992) The nature of zircon inheritance in two granite plutons. In: Brown PE, Chappell BW (eds) The Second Hutton Symposium on the Origin of Granites and Related Rocks. Geological Society of America, Boulder, pp 459–471 https://doi.org/10.1130/SPE272-p459

Paul AN, Spikings RA, Ulianov A, Ovtcharova M (2018) High temperature (>350°C) thermal histories of the long lived (>500 Ma) active margin of Ecuador and Colombia: Apatite, titanite and rutile U-Pb thermochronology. Geochim Cosmochim Acta 228:275–300. https://doi.org/10.1016/j.gca.2018.02.033

Petford N, Cruden AR, McCaffrey KJW, Vigneresse J-L (2000) Granite magma formation, transport and emplacement in the Earth's crust. Nature 408:669–673. https://doi.org/10.1038/35047000

Reichardt H, Weinberg RF (2012) The dike swarm of the Karakoram shear zone, Ladakh, NW India: Linking granite source to batholith. Geol Soc Am Bull 124:89–103. https://doi.org/10.1130/B30394.1

Riel N, Guillot S, Jaillard E, Martelat J-E, Paquette J-L, Schwartz S, Goncalves P, Duclaux G, Thebaud N, Lanari P, Janots E, Yuquilema J (2013) Metamorphic and geochronogical study of the Triassic El Oro metamorphic complex, Ecuador: Implications for high-temperature metamorphism in a forearc zone. Lithos 156–159:41–68. https://doi.org/10.1016/j.lithos.2012.10.005

Riel N, Martelat J-E, Guillot S, Jaillard E, Monié P, Yuquilema J, Duclaux G, Mercier J (2014) Fore arc tectonothermal evolution of the El Oro metamorphic province (Ecuador) during the Mesozoic. Tectonics 33:1989–2012. https://doi.org/10.1002/2014TC003618

Riel N, Mercier J, Weinberg R (2016) Convection in a partially molten metasedimentary crust? Insights from the El Oro complex (Ecuador). Geology 44:31–34. https://doi.org/10.1130/G37208.1

Roberts MP, Finger F (1997) Do U-Pb zircon ages from granulites reflect peak metamorphic conditions? Geology 25:319. https://doi.org/10.1130/0091-7613

Roberts N, Yakymchuk C, Spencer CJ, Keller CB, Tapster SR (2024) Revisiting the discrimination and distribution of S-type granites from zircon trace element composition. Earth Planet Sci Lett 633:118638. https://doi.org/10.1016/j.epsl.2024.118638

Rousseeuw PJ, Croux C (1993) Alternatives to the Median Absolute Deviation. J Am Stat Assoc 88:1273–1283. https://doi.org/10.1080/01621459.1993.10476408

Rubatto D (2002) Zircon trace element geochemistry: partitioning with garnet and the link between U–Pb ages and metamorphism. Chem Geol 184:123–138. https://doi.org/10.1016/S0009-2541(01)00355-2

Rubatto D (2017) Zircon: The Metamorphic Mineral. Rev Mineral Geochem 83:261–295. https://doi.org/10.2138/rmg.2017.83.9

Rubatto D, Williams IS, Buick IS (2001) Zircon and monazite response to prograde metamorphism in the Reynolds Range, central Australia. Contrib Mineral Petrol 140:458–468. https://doi.org/10.1007/PL00007673

Rubatto D, Hermann J, Buick IS (2006) Temperature and Bulk Composition Control on the Growth of Monazite and Zircon During Low-pressure Anatexis (Mount Stafford, Central Australia). J Petrol 47:1973–1996. https://doi.org/10.1093/petrology/egl033

Rubatto D, Hermann J, Berger A, Engi M (2009) Protracted fluid-induced melting during Barrovian metamorphism in the Central Alps. Contrib Mineral Petrol 158:703–722. https://doi.org/10.1007/s00410-009-0406-5

Rubatto D, Chakraborty S, Dasgupta S (2013) Timescales of crustal melting in the Higher Himalayan Crystallines (Sikkim, Eastern Himalaya) inferred from trace element-constrained monazite and zircon chronology. Contrib Mineral Petrol 165:349–372. https://doi.org/10.1007/s00410-012-0812-y

Samperton KM, Schoene B, Cottle JM, Brenhin Keller C, Crowley JL, Schmitz MD (2015) Magma emplacement, differentiation and cooling in the middle crust: Integrated zircon geochronological–geochemical constraints from the Bergell Intrusion, Central Alps. Chem Geol 417:322–340. https://doi.org/10.1016/j.chemgeo.2015.10.024

Sawyer EW (2008) Atlas of migmatites. NRC research, Ottawa

Sawyer EW, Cesare B, Brown M (2011) When the Continental Crust Melts. Elements 7:229–234. https://doi.org/10.2113/gselements.7.4.229

Schaltegger U, Fanning CM, Günther D, Maurin JC, Schulmann K, Gebauer D (1999) Growth, annealing and recrystallization of zircon and preservation of monazite in high-grade metamorphism: conventional and in-situ U-Pb isotope, cathodoluminescence and microchemical evidence. Contrib Mineral Petrol 134:186–201. https://doi.org/10.1007/s004100050478

Schiller D, Finger F (2019) Application of Ti-in-zircon thermometry to granite studies: problems and possible solutions. Contrib Mineral Petrol 174:51. https://doi.org/10.1007/s00410-019-1585-3

Schmitt AK, Sliwinski J, Caricchi L, Bachmann O, Riel N, Kaus BJP, Cisneros De Léon A, Cornet J, Friedrichs B, Lovera O, Sheldrake T, Weber G (2023) Zircon age spectra to quantify magma evolution. Geosphere 19:1006–1031. https://doi.org/10.1130/GES02563.1

Schoene B, Schaltegger U, Brack P, Latkoczy C, Stracke A, Günther D (2012) Rates of magma differentiation and emplacement in a ballooning pluton recorded by U–Pb TIMS-TEA, Adamello batholith, Italy. Earth Planet Sci Lett 355–356:162–173. https://doi.org/10.1016/j.epsl.2012.08.019

Sláma J, Košler J, Condon DJ, Crowley JL, Gerdes A, Hanchar JM, Horstwood MSA, Morris GA, Nasdala L, Norberg N, Schaltegger U, Schoene B, Tubrett MN, Whitehouse MJ (2008) Plešovice zircon — A new natural reference material for U–Pb and Hf isotopic microanalysis. Chem Geol 249:1–35. https://doi.org/10.1016/j.chemgeo.2007.11.005

Sliwinski JT, Guillong M, Horstwood MSA, Bachmann O (2022) Quantifying Long-Term Reproducibility of Zircon Reference Materials by U-Pb LA-ICP-MS Dating. Geostand Geoanalytical Res 46:401–409. https://doi.org/10.1111/ggr.12442

Spandler C, Hammerli J, Sha P, Hilbert-Wolf H, Hu Y, Roberts E, Schmitz M (2016) MKED1: A new titanite standard for in situ analysis of Sm–Nd isotopes and U–Pb geochronology. Chem Geol 425:110–126. https://doi.org/10.1016/j.chemgeo.2016.01.002

Sparks RSJ, Annen C, Blundy JD, Cashman KV, Rust AC, Jackson MD (2019) Formation and dynamics of magma reservoirs. Philos Trans R Soc Math Phys Eng Sci 377:20180019. https://doi.org/10.1098/rsta.2018.0019

Spear FS, Parrish RR (1996) Petrology and Cooling Rates of the Valhalla Complex, British Columbia. Can J Petrol 37:733–765. https://doi.org/10.1093/petrology/37.4.733

Spikings R, Cochrane R, Villagomez D, Van Der Lelij R, Vallejo C, Winkler W, Beate B (2015) The geological history of northwestern South America: from Pangaea to the early collision of the Caribbean Large Igneous Province (290–75 Ma). Gondwana Res 27:95–139. https://doi.org/10.1016/j.gr.2014.06.004

Stacey JS, Kramers JD (1975) Approximation of terrestrial lead isotope evolution by a two-stage model. Earth Planet Sci Lett 26:207–221. https://doi.org/10.1016/0012-821X(75)90088-6

Stearns MA, Cottle JM, Hacker BR, Kylander-Clark ARC (2016) Extracting thermal histories from the near-rim zoning in titanite using coupled U-Pb and trace-element depth profiles by single-shot laser-ablation split stream (SS-LASS) ICP-MS. Chem Geol 422:13–24. https://doi.org/10.1016/j.chemgeo.2015.12.011

Suhr N, Rojas-Agramonte Y, Chew DM, Pinto AJ, Villagómez-Díaz D, Toulkeridis T, Mertz-Kraus R (2019) Detrital-zircon geochronology and provenance of the El Oro Metamorphic Complex, Ecuador: Geodynamic implications for the evolution of the western Gondwana margin. J South Am Earth Sci 90:520–539. https://doi.org/10.1016/j.jsames.2018.12.010

Szymanowski D, Ellis BS, Bachmann O, Guillong M, Phillips WM (2015) Bridging basalts and rhyolites in the Yellowstone–Snake River Plain volcanic province: The elusive intermediate step. Earth Planet Sci Lett 415:80–89. https://doi.org/10.1016/j.epsl.2015.01.041

Szymanowski D, Ellis BS, Wotzlaw J-F, Bachmann O (2019) Maturation and rejuvenation of a silicic magma reservoir: High-resolution chronology of the Kneeling Nun Tuff. Earth Planet Sci Lett 510:103–115. https://doi.org/10.1016/j.epsl.2019.01.007

Szymanowski D, Forni F, Wolff JA, Ellis BS (2020) Modulation of zircon solubility by crystal–melt dynamics. Geology 48:798–802. https://doi.org/10.1130/G47405.1

Taylor RJM, Kirkland CL, Clark C (2016) Accessories after the facts: Constraining the timing, duration and conditions of high-temperature metamorphic processes. Lithos 264:239–257. https://doi.org/10.1016/j.lithos.2016.09.004

Tedeschi M, Pedrosa-Soares A, Dussin I, Lanari P, Novo T, Pinheiro MAP, Lana C, Peters D (2018) Protracted zircon geochronological record of UHT garnet-free granulites in the Southern Brasília orogen (SE Brazil): Petrochronological constraints on magmatism and metamorphism. Precambrian Res 316:103–126. https://doi.org/10.1016/j.precamres.2018.07.023

Trail D, Bruce Watson E, Tailby ND (2012) Ce and Eu anomalies in zircon as proxies for the oxidation state of magmas. Geochim Cosmochim Acta 97:70–87. https://doi.org/10.1016/j.gca.2012.08.032

Tucker RD, Robinson P, Solli A, Gee DG, Thorsnes T, Krogh TE, Nordgulen Ø, Bickford M (2004) Thrusting and extension in the Scandian hinterland, Norway: New U-Pb ages and tectonostratigraphic evidence. Am J Sci 304:477–532. https://doi.org/10.2475/ajs.304.6.477

Valley JW (2003) Oxygen isotopes in zircon. Rev Mineral Geochem 53:343–385 https://doi.org/10.2113/0530343

Van Zalinge ME, Mark DF, Sparks RSJ, Tremblay MM, Keller CB, Cooper FJ, Rust A (2022) Timescales for pluton growth, magma-chamber formation and super-eruptions. Nature 608:87–92. https://doi.org/10.1038/s41586-022-04921-9

Vermeesch P (2018) IsoplotR: A free and open toolbox for geochronology. Geosci Front 9:1479–1493. https://doi.org/10.1016/j.gsf.2018.04.001

Vielzeuf D, Clemens JD, Pin C, Moinet E (1990) Granites, Granulites, and Crustal Differentiation. In: Vielzeuf D, Vidal, Ph (eds) Granulites and Crustal Evolution. Springer Netherlands, Dordrecht, pp 59–85 https://doi.org/10.1007/978-94-009-2055-2_5

Vinasco Vallejo CJ (2004) Evolução crustal e história tectônica dos granitóides permo-triássicos dos Andes do Norte. Doutorado em Geoquímica e Geotectônica, Universidade de São Paulo

Warr LN (2021) IMA–CNMNC approved mineral symbols. Mineral Mag 85:291–320. https://doi.org/10.1180/mgm.2021.43

Watson EB, Harrison TM (1983) Zircon saturation revisited: temperature and composition effects in a variety of crustal magma types. Earth Planet Sci Lett 64:295–304. https://doi.org/10.1016/0012-821X(83)90211-X

Wei C-S, Zhao Z-F, Spicuzza MJ (2008) Zircon oxygen isotopic constraint on the sources of late Mesozoic A-type granites in eastern China. Chem Geol 250:1–15. https://doi.org/10.1016/j.chemgeo.2008.01.004

Weinberg RF (2016) Himalayan leucogranites and migmatites: nature, timing and duration of anatexis. J Metamorph Geol 34:821–843. https://doi.org/10.1111/jmg.12204

Wiedenbeck M, Alle P, Corfu F, Griffin W, Meier M, Oberli F, von v, Quadt A, Roddick J, Spiegel W (1995) Three natural zircon standards for U-Th-Pb, Lu-Hf, trace element and REE analyses. Geostand Newsl 19:1–23. https://doi.org/10.1111/j.1751-908X.1995.tb00147.x

Winter JD (2014) Principles of igneous and metamorphic petrology, 2. ed., Pearson new internat. ed. Pearson Education, Harlow https://doi.org/10.1017/CBO9780511813429

Wotzlaw J-F, Schaltegger U, Frick DA, Dungan MA, Gerdes A, Günther D (2013) Tracking the evolution of large-volume silicic magma reservoirs from assembly to supereruption. Geology 41:867–870. https://doi.org/10.1130/G34366.1

Wu F-Y, Sun D-Y, Ge W-C, Zhang Y-B, Grant ML, Wilde SA, Jahn B-M (2011) Geochronology of the Phanerozoic granitoids in northeastern China. J Asian Earth Sci 41:1–30. https://doi.org/10.1016/j.jseaes.2010.11.014

Yakymchuk C (2023) Prograde zircon growth in migmatites. J Metamorph Geol 41:719–743. https://doi.org/10.1111/jmg.12715

Yakymchuk C, Kirkland CL, Clark C (2018) Th/U ratios in metamorphic zircon. J Metamorph Geol 36:715–737. https://doi.org/10.1111/jmg.12307

Yang J-H, Wu F-Y, Wilde SA, Xie L-W, Yang Y-H, Liu X-M (2006) Tracing magma mixing in granite genesis: in situ U–Pb dating and Hf-isotope analysis of zircons. Contrib Mineral Petrol 153:177–190. https://doi.org/10.1007/s00410-006-0139-7

Kohn, M.J. and Kelly, N.M. (2018). Petrology and Geochronology of Metamorphic Zircon. In Microstructural Geochronology (eds D.E. Moser, F. Corfu, J.R. Darling, S.M. Reddy and K. Tait) https://doi.org/10.1002/9781119227250.ch2

Publisher's Note Springer Nature remains neutral with regard to jurisdictional claims in published maps and institutional affiliations.